Dynamic inter-domain transformations mediate the allosteric regulation of human 5, 10-methylenetetrahydrofolate reductase

Linnea K. M. Blomgren[1], Melanie Huber[1], Sabrina R. Mackinnon[2], Céline Bürer[1], Arnaud Baslé[2], Wyatt W. Yue[2,3] ✉, D. Sean Froese[1] ✉, Thomas J. McCorvie[2] ✉

[1]Division of Metabolism and Children's Research Center, University Children's Hospital Zürich, University of Zürich, Zürich, Switzerland

[2]Biosciences Institute, The Medical School, Newcastle University, Newcastle upon Tyne, NE2 4HH, UK

[3]Centre for Medicines Discovery, Nuffield Department of Clinical Medicine, University of Oxford, Oxford, OX3 7DQ, UK

✉e-mail: Wyatt.Yue@newcastle.ac.uk; Sean.Froese@kispi.uzh.ch; Thomas.McCorvie@newcastle.ac.uk

One-carbon metabolism drives an extensive network of signalling and biosynthetic pathways essential for cell growth and redox regulation. In all domains of life, 5,10-methylenetetrahydrofolate reductase (MTHFR) signals the commitment of folate-derived one-carbon units into biosynthesis of the global donor of trans-methylation, S-adenosyl-L-methionine (SAM). Eukaryotic MTHFR appends to its conserved TIM-barrel catalytic domain (CD) a unique regulatory domain (RD) that confers feedback inhibition by SAM. We determined, through cryo-electron microscopy, multiple structures of human MTHFR bound to SAM, and its demethylated product S-adenosyl-L-homocysteine (SAH) that relieves SAM inhibition. In the active SAH-bound state, the CD is flexible and its active site accessible for catalysis. SAM binding in the inhibited state substantially rearranges the inter-domain linker, which: remodels the RD pocket, reorients the CD, inserts a loop from the linker into the CD blocking active site access, and mobilizes Tyr404 to lock onto the flavin adenine dinucleotide cofactor. The switch between the active and inhibited states is facilitated by binding of either one SAH or two SAM molecules to the RD, respectively. Occupation of both SAM sites is required for inhibition, but the second site is occluded in the presence of SAH. Together our data explain the long-distance inhibitory mechanism of MTHFR employed by dual SAM binding, demonstrate how a single bound SAH confers a dis-inhibitory signal, and pave the way for rational design of novel therapeutics targeting MTHFR.

S-adenosyl-L-methionine (SAM) is the most important methyl group donor of the cell. It facilitates over 200 transmethylation reactions that modify DNA, RNA, proteins, and metabolites[1]. Indeed, SAM is the most widely used cellular co-substrate after ATP, and the ratio of SAM to its demethylated product SAH serves as an index of the cell's methylation potential[2], driving the myriad of transmethylation reactions in cells and tissues. In humans, SAM synthesis proceeds through adenosylation of methionine, whose precursor is homocysteine. This process requires the folate derivative 5-methyltetrahydrofolate (CH_3-THF), generated solely by the enzyme 5,10-methylenetetrahydrofolate reductase (MTHFR) from 5,10-methylenetetrahydrofolate (CH_2-THF)[3]. In so doing, MTHFR represents the first committed step to SAM biosynthesis, shuttling one-carbon units in the form of CH_2-THF away from nucleotide synthesis. MTHFR dysfunction therefore has an enormous impact in human health, and has been associated with cancer[4,5], cardiovascular disease[6,7], and neural tube defects[8,9]. Notably, severe MTHFR deficiency, due to inherited bi-allelic disease-causing variants in the *MTHFR* gene, is a rare autosomal recessive disorder resulting from a loss of enzymatic function, which leads to homocystinuria and can be fatal if left untreated[10].

MTHFR can be found in all domains of life. In contrast to prokaryotes, eukaryotes have evolved an elegant feedback regulation mechanism to modulate MTHFR activity. Human MTHFR is exquisitely sensitive to the SAM:SAH ratio, being allosterically inhibited by SAM[11,12] and re-activated by SAH[13,14]. The sensitivity of MTHFR towards SAM inhibition is also modulated by multiple Ser/Thr phosphorylations[15] , whereby phosphorylated MTHFR has a reduced Ki for SAM and thus is poised for the inhibited state[16]. Our recently determined crystal structure of human MTHFR, in complex with SAH, revealed a two-domain enzyme architecture[16]. The catalytic domain (CD), composed of a TIM-barrel fold conserved across all species[16], binds the cofactor FAD, the electron donor nicotinamide adenine dinucleotide phosphate (NADPH) and the substrate methylenetetrahydrofolate (CH_2-THF), such that physiologically the forward activity leading to CH_3-THF formation takes place[17,18]. This CD is appended to a structurally unique regulatory domain (RD) via an extended inter-domain linker. The RD contains the binding pocket for SAH, and expectedly for SAM also. Combined crystallographic, small angle X-ray scattering (SAXS), and native MS studies revealed significant intrinsic flexibility, particularly with respect to inter-domain orientations[16]. Such conformational flexibility of MTHFR is consistent with its complex regulatory mechanism, which remains to be characterised in molecular detail.

The catalytic mechanism of the MTHFR reaction towards forming CH_3-THF is well understood, through the plethora of structural and enzymatic studies from diverse orthologous proteins[3,19–22]; however, little is known about how this activity is allosterically regulated in eukaryotic enzymes. The binding of SAM and SAH to the RD have been suggested to induce different MTHFR conformers that correspond to the inhibited and dis-inhibited states, respectively[16]. Nevertheless, how this is related to the dimeric structure of MTHFR and the signal transduction within the monomers has not yet been characterized. To answer these questions, we have subjected full-length human MTHFR incubated with SAM or SAH to cryo-electron microscopy (cryo-EM). The multiple structures determined give new insights into the large conformational changes necessary for MTHFR allosteric regulation. In combination with functional assays, our structures present an unexpected discrepancy in the binding stoichiometry of SAM and SAH, and detail how SAM binding remodels the allosteric pocket and induces structural rearrangements of the inter-domain linker that are key to mediating the conformational states of MTHFR.

Inter-domain rearrangement of MTHFR in response to SAM/SAH

The crystal structure of human MTHFR[16], derived from a non-phosphorylatable truncation construct ($MTHFR_{trunc}$ aa 38-644), may not reflect the full capability of the protein in its conformational dynamics during catalysis and regulation. Therefore, we pursued structural studies using the full-length protein ($MTHFR_{FL}$ aa 1-656) that harbours the N-terminal Ser/Thr-rich region and is multiply phosphorylated during its recombinant expression (Fig. 1a). Initial negative stain electron microscopy revealed 2D classes consisting of four or three lobes. Two distinct types of classes were present when the protein was incubated with either SAH or SAM (Extended Data Fig. 1a,b). One type of 2D classes showed an extended conformation of the MTHFR homodimer, possibly corresponding to the $MTHFR_{trunc}$ crystal structure complexed with SAH that triggered a dis-inhibited state of the enzyme (PDB:6fcx). The other type of 2D classes exhibited a more compact conformation and appeared to be dimeric MTHFR with different domain orientations, possibly representing an inhibited state of MTHFR triggered by the presence of SAM.

Prompted by the possibility to investigate both SAM- and SAH-induced conformers from the full-length protein sample, we proceeded with cryo-EM data collections to gain higher resolution structures. $MTHFR_{FL}$ protein suffered from some orientation bias on grids, which we overcame by the application of C2 symmetry in refinements (Table 1 and Extended Data

Figs. 2a-h, 3a-e, and 4). We also combined particles from different grids to diversify any captured views[23]. A combination of global and masked local refinements with symmetry expansion resulted in three maps ranging from 2.8 – 3.1 Å resolution that allowed us to confidently model both the SAH- and SAM-bound states of MTHFR.

In the presence of excess SAH (~100-fold relative to protein), a concentration at which MTHFR is fully active (Extended Data Fig. 5a), a masked local refinement at 2.8 Å resolution allowed a reconstruction ($MTHFR_{FL}^{SAH\ (symm)}$) of the MTHFR homodimeric interface involving the two RDs. This is highly analogous to the SAH-bound $MTHFR_{trunc}$ crystal structure (C^{α}-RMSD 0.627 Å), with respect to the dimer packing arrangement, as well as the placement and orientation of one SAH molecule within the RD pocket (Extended Data Figs. 2a-e and 5b). Beyond the RD, however, there is high flexibility in the linker and CD regions in our locally refined map. This is strongly reflected in an asymmetric map at 3.1 Å resolution ($MTHFR_{FL}^{SAH\ (asymm)}$) obtained from symmetry expansion and 3D classification (Fig. 1b and Extended Data Fig. 2a,b,f-h). Here, the MTHFR homodimers appeared as asymmetric particles, where for one protomer both the linker and CD are highly disordered. In contrast, density was present for the linker and CD of the other protomer, though the density of both suggested some amount of flexibility (Fig. 1b,c and Extended Data Fig. 5c). The CD-RD orientation and conformational asymmetry across protomers seen here agree with that of the SAH-bound crystal structure (Extended Data Fig. 5b). Considered together, our SAH-bound structures are consistent with the notion that SAH renders the MTHFR protein to be active, whereby the CDs are highly flexible and provide unhindered access of the substrate CH_2-THF and electron donor NADPH to the active site for catalysis.

Following incubation with 500-fold excess SAM, a ligand concentration where MTHFR is fully inhibited (Extended Data Fig. 5a), we determined one map at 2.9 Å resolution with C2 symmetry applied (Fig. 1b and Extended Data Fig. 3a-e). The high quality of the map allowed us to model the bulk of the CD (aa 44-160, 171-341), part of the linker region (380-412), and the near entirety of the RD (aa 413-644) (Fig. 1a,b). It is immediately apparent that this SAM-induced structure ($MTHFR_{FL}^{SAM}$) adopts drastically different inter-domain orientations compared to the SAH-bound cryo-EM ($MTHFR_{FL}^{SAH\ (asymm)}$, this study) and crystal ($MTHFR_{trunc}$[16] structures. By overlaying these structures using the homodimeric RD interface (C^{α}-RMSD 0.827 Å) (Extended Data Fig. 5d), we observed a significant rigid body movement of each CD relative to its own RD (Fig. 1b). This inter-domain rearrangement manifests as a ~34° rotation coupled to ~14.8 Å translation, along an axis that intersects with the linker region connecting the CD and RD (Extended Data Fig. 5e). Such a conformational change is consistent with our negative stain 2D classes (Extended Data Fig. 1a,b) and is reflected by both FAD emission and differential scanning fluorimetry (DSF) experiments. Here 1 mM SAM resulted in a 3-4°C increase in the melting temperature of as-purified MTHFR, whereas incubation with SAH resulted in no increase in stability (Extended Data Fig. 5f and Supplementary Fig. 1). This two-state transition, which essentially displaces the CD active site by nearly 30 Å (Fig. 1c), can be likened to the opening and closing of an oyster shell that controls the accessibility of its shell content (i.e. the active site) (Fig. 1d). As a result, the CD rotation narrows the cleft between the domains and traps the linker between them.

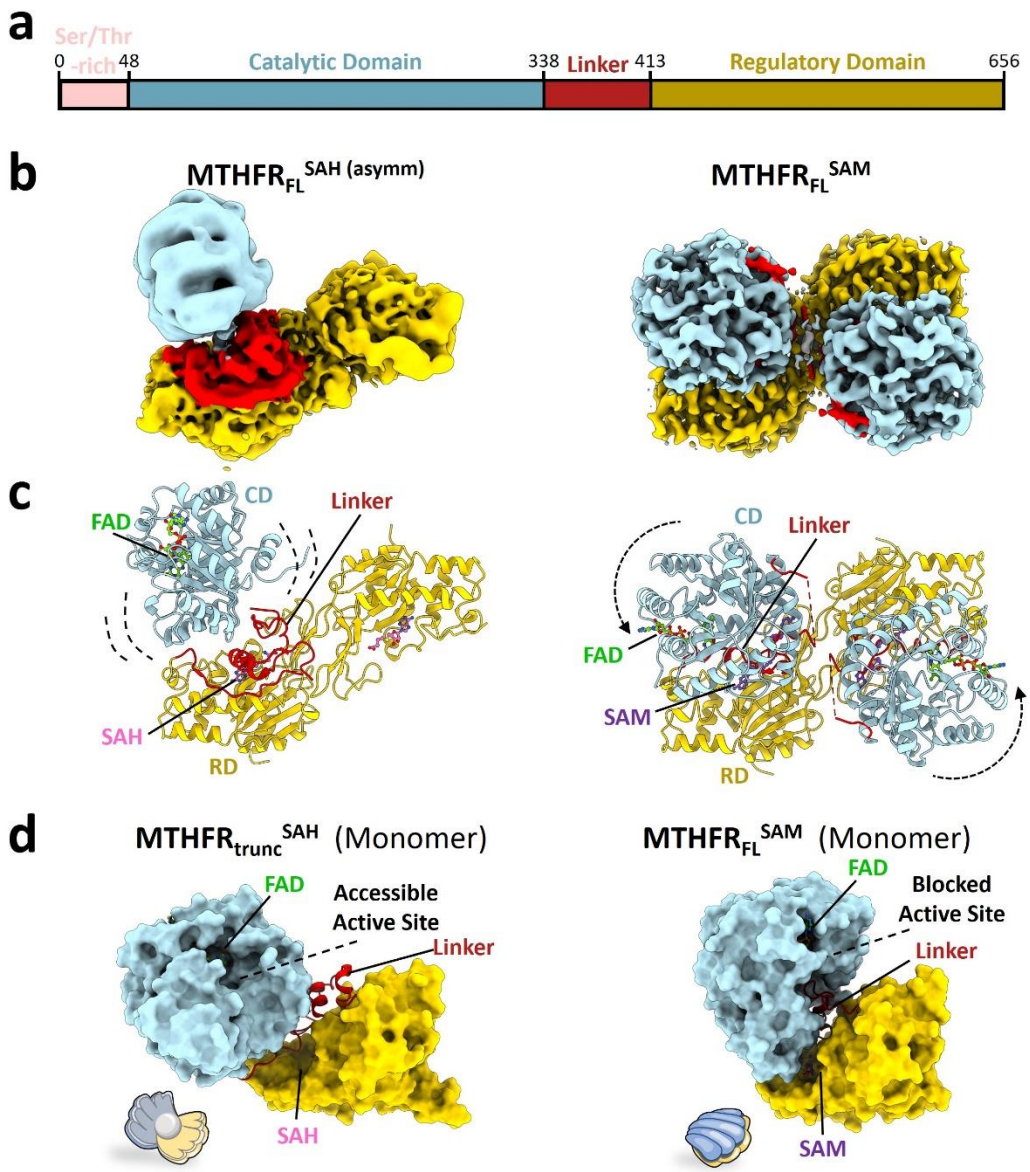

Fig. 1 | Conformational change from open SAH-bound to closed SAM-bound MTHFR$_{FL}$. **a,** Schematic representation of full-length human MTHFR$_{FL}$, used for cryo-EM experiments and coloured according to protein domain. The colour coding is maintained in subsequent structural representations. **b-c**, Cryo-EM maps (**b**) and corresponding molecular models (**c**) of MTHFR$_{FL}^{SAH\ (asymm)}$ (left) and MTHFR$_{FL}^{SAM}$ (right). Note the rigid body displacement and rotation of the CD with respect to the rigid RD in MTHFR$_{FL}^{SAM}$ (represented by dashed arrows). Identified ligands are indicated in **c**. **d**, Surface representation of monomeric MTHFR$_{trunc}^{SAH}$ (left), with accessible active site resembling an open oyster shell, and monomeric MTHFR$_{FL}^{SAM}$ (right) with a closed interdomain arrangement and limited access to the active site resembling a closed oyster shell.

Steric blockage of the active site from linker insertion causes allosteric inhibition

MTHFR across all domains of life retains a common binding site for the electron donor NAD(P)H and substrate CH_2-THF at the entrance of the CD active site[16,19,20,24]. As part of the bi-bi ping-pong catalytic mechanism[24,25], NAD(P)H (Fig. 2a) and CH_2-THF (Fig. 2b) stack against the flavin cofactor FAD in turn to carry out hydride transfer reactions. In our

$MTHFR_{FL}^{SAM}$ structure, FAD was found in both CD active sites of the homodimer (Fig. 2c) with clear electron densities (Extended Data Fig. 6a), which superimpose well with those found in $MTHFR_{trunc}^{SAH}$ and orthologue structures (Extended Data Fig. 6b).

Notably, the direct consequence of the inter-domain rearrangement in the presence of SAM is that the CD active site is now oriented towards a different environment of the linker and RD regions (Fig. 2d). To our surprise, the entrance to the CD active site of $MTHFR_{FL}^{SAM}$ is blocked by a hydrophobic insertion of the linker region, bringing in three aromatic residues from a $Y_{403}YLF_{406}$ sequence (Tyr403, Tyr404, Phe406) to fill the space where NADPH/CH_2-THF is expected to bind (Fig. 2c). In addition to occluding the active site entrance, the linker residue Tyr404 mimics NADPH and CH_2-THF through π-π stacking with the FAD isoalloxazine ring, in addition to interacting with Glu63, Thr94, and Tyr321 (Extended Data Fig. 6b) – strongly/strictly conserved residues across all kingdoms of life[16] – that are involved in CH_2-THF and NAD(P)H binding (Fig. 2a,b and Extended Data Fig. 6b). The hydrophobic insertion is further accommodated in the CD through a reorientation of helix α8, which flanks the NADPH/CH_2-THF binding site. Here, helix α8 is displaced away from its position in $MTHFR_{trunc}^{SAH}$ and re-oriented towards the exterior (Fig. 2c and Extended Data Fig. 6c). As a result, residues Lys270, Leu271, and Ser272 of helix α8, which are conserved from mammals to worms (Supplementary Fig. 2) and previously implicated in differentiating specificity between NADH (electron donor in bacterial MTHFRs)[26] and NADPH (electron donor in eukaryotic MTHFRs)[16], have been displaced by ~7 Å to make way for the hydrophobic insertion. The sidechain of Lys273, which would otherwise interact with CH_2-THF/NADPH, is also directed away from the binding site (Extended Data Fig. 6c).

The hydrophobic $Y_{403}YLF_{406}$ insertion from the linker therefore represents an auto-inhibitory element sterically blocking the NADPH/CH_2-THF binding site in a competitive manner. The essentiality of the steric inhibition by the key insertion residue Tyr404 is underlined by its substitution to Ala404, which ablated SAM-induced inhibition (Fig. 2e) but importantly did not compromise the maximal activity of the enzyme (Extended Data Fig. 6d). This implies that the insertion does not modify the active site *per se*; instead, the approximately 10 Å movement and rotation of Tyr404 (Fig. 2f) enables it to both plug the active site and fasten itself to the FAD, in a ‘block-and-lock’ fashion.

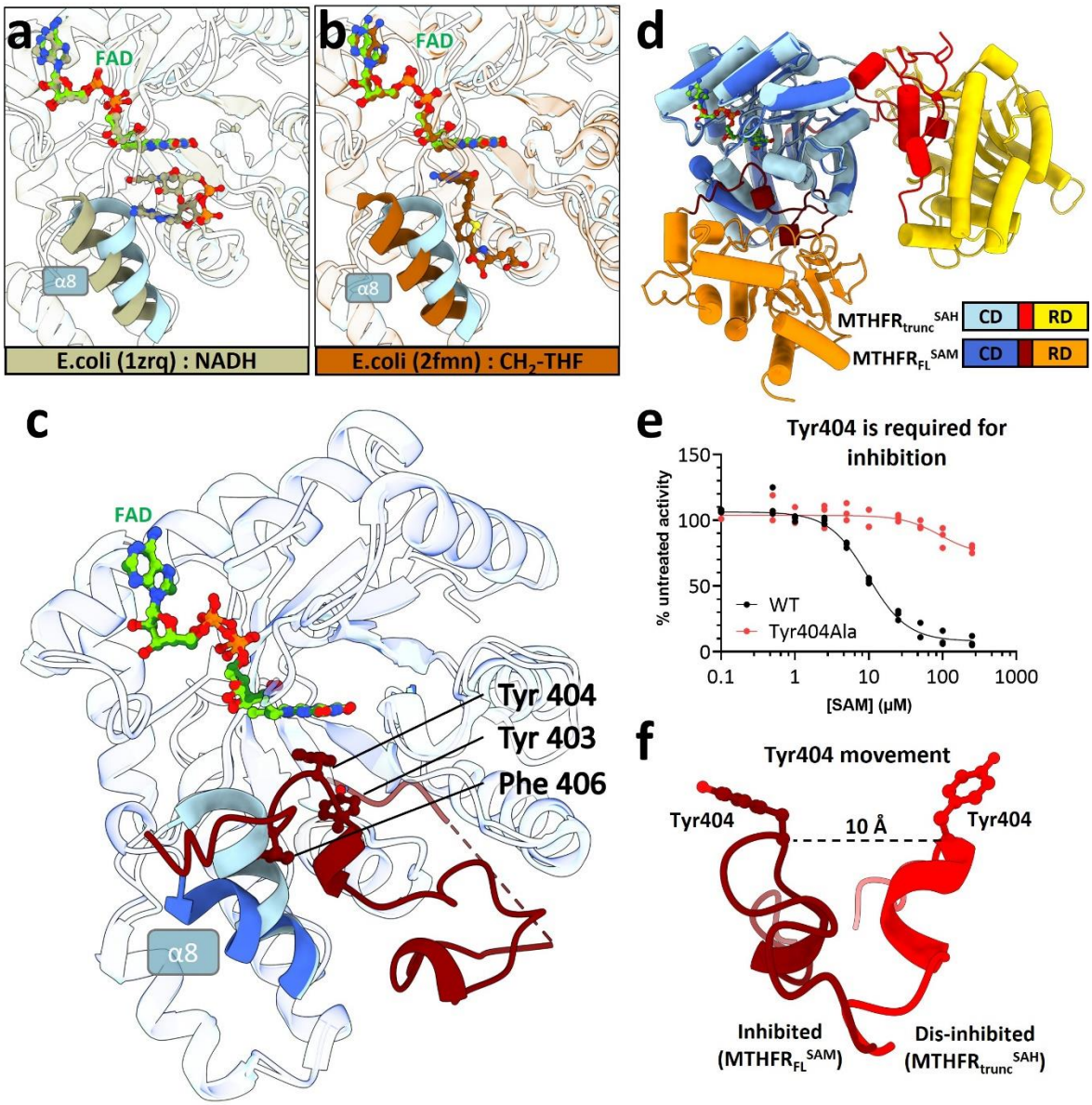

Fig. 2 | $MTHFR_{FL}^{SAM}$ reveals steric hindrance of the active site by hydrophobic linker insertion. **a-b,** Zoomed view of the active site for $MTHFR_{trunc}^{SAH}$ overlayed with crystal structures of *Escherichia coli* MTHFR homologues to highlight stacking interactions of FAD with NADH (**a**, PDB: 1zrq[24]), and 5,10-methylenetetrahydrofolate (CH_2-THF) (**b**, PDB: 2fmn[20]). **c**, Overlay of the CD of $MTHFR_{trunc}^{SAH}$ (light blue) and $MTHFR_{FL}^{SAM}$ (dark blue). Note the movement of helix α8 to accommodate the hydrophobic insertion of linker residues Tyr403, Tyr404, and Phe406 in $MTHFR_{FL}^{SAM}$ (dark red). In **a-c** white ribbons represent complete superposition. **d**, Tube cartoon representation of monomeric $MTHFR_{trunc}^{SAH}$ and $MTHFR_{FL}^{SAM}$ aligned with respect to the CD. **e**, Relative enzymatic activity of $MTHFR_{FL}$ protein following incubation with SAM. WT and Tyr404Ala $MTHFR_{FL}$ were overexpressed in HEK293T MTHFR knock-out cells and measured as lysates. N=3 biological replicates. **f**, Comparison of the position of Tyr404 in $MTHFR_{trunc}^{SAH}$ (red) and $MTHFR_{FL}^{SAM}$ (dark red) illustrating the side-chain rotation and ~10 Å shift in position.

Mobility of the linker drives the inter-domain reorientation

The transition of MTHFR from the open, dis-inhibited conformer (in the presence of SAH) to the closed, inhibited conformer (in the presence of SAM), resulting in the CD-RD re-orientation and steric insertion, is facilitated by an extensive rearrangement of the linker connecting the two domains. Based on the $MTHFR_{trunc}^{SAH}$ crystal structure, the linker was expected to comprise aa 338-362[16]. With the determination of $MTHFR_{FL}^{SAM}$, we have redefined a more extended linker, comprising three adjoining segments (LS1: aa 338-380, LS2: aa 381-393, LS3: aa 394-412), which display significant mobility (Fig. 3a).

The first linker segment (LS1) was not possible to model in both $MTHFR_{FL}^{SAM}$ protomers and one protomer of $MTHFR_{FL}^{SAH\ (asymm)}$, indicating high intrinsic flexibility and disorder. In the $MTHFR_{trunc}^{SAH}$ crystal structure, however, this region adopts an α-helix (α12) and stabilises the SAH in its RD binding pocket through a β-turn contributing Arg345 and Pro348 to abut the SAH homocysteine moiety, as well as through the connection between strand β9 and helix α12 to position Ala368 into proximity with the SAH sulphonium (Fig. 3b,c and Extended Data Fig. 7a,b).

The second (LS2) and third (LS3) linker segments were previously interpreted to constitute part of the RD, connecting α12 and α13 in the $MTHFR_{trunc}^{SAH}$ structure[16] . In $MTHFR_{FL}^{SAM}$, however, these two segments undergo substantial flexing to a different trajectory (average C^{α}-RMSD 10.87Å). Composed of a 12-residue turn, LS2 swings from its position in $MTHFR_{trunc}^{SAH}$, where it interacts with its equivalent in the $MTHFR_{trunc}^{SAH}$ homodimeric interface (Fig. 3b and Extended Data Fig. 7a,c), to a position of penetrating and remodelling the RD binding pocket in $MTHFR_{FL}^{SAM}$ (Fig. 3d,e and Extended Data Fig. 7d), as described further in the next section. This segment harbours the motif $F_{384}PNGRW_{389}$, which is strongly conserved across all eukaryotes (Supplementary Fig. 2). To validate the importance of this motif, we performed alanine substitution of Phe384, Asn386, Arg388 and Trp389, each of which reduced enzymatic activity by 30-50% compared to wild-type MTHFR (Extended Data Fig. 7e). This underscores the necessity of the turn for fully functional MTHFR activity.

LS3 harbours the auto-inhibitory element $Y_{403}YLF_{406}$ including the insertion residue Tyr404. In $MTHFR_{trunc}^{SAH}$, this segment resides against the long helix α17 outside of the RD core (Fig. 3b and Extended Data Fig. 7b). In $MTHFR_{FL}^{SAM}$ LS3 is drastically rearranged to adopt a position that packs closer to the CD and threads along the floor of the NADPH/CH_2-THF pocket in the CD (Fig. 3d and Extended Data Fig. 7d). This substantive displacement accounts for the long distance travelled by the insertion residue Tyr404 (10 Å), as well as the re-orientation of its aromatic sidechain (Fig. 2f), both of which are required for its steric blockage of the NADPH/CH_2-THF pocket.

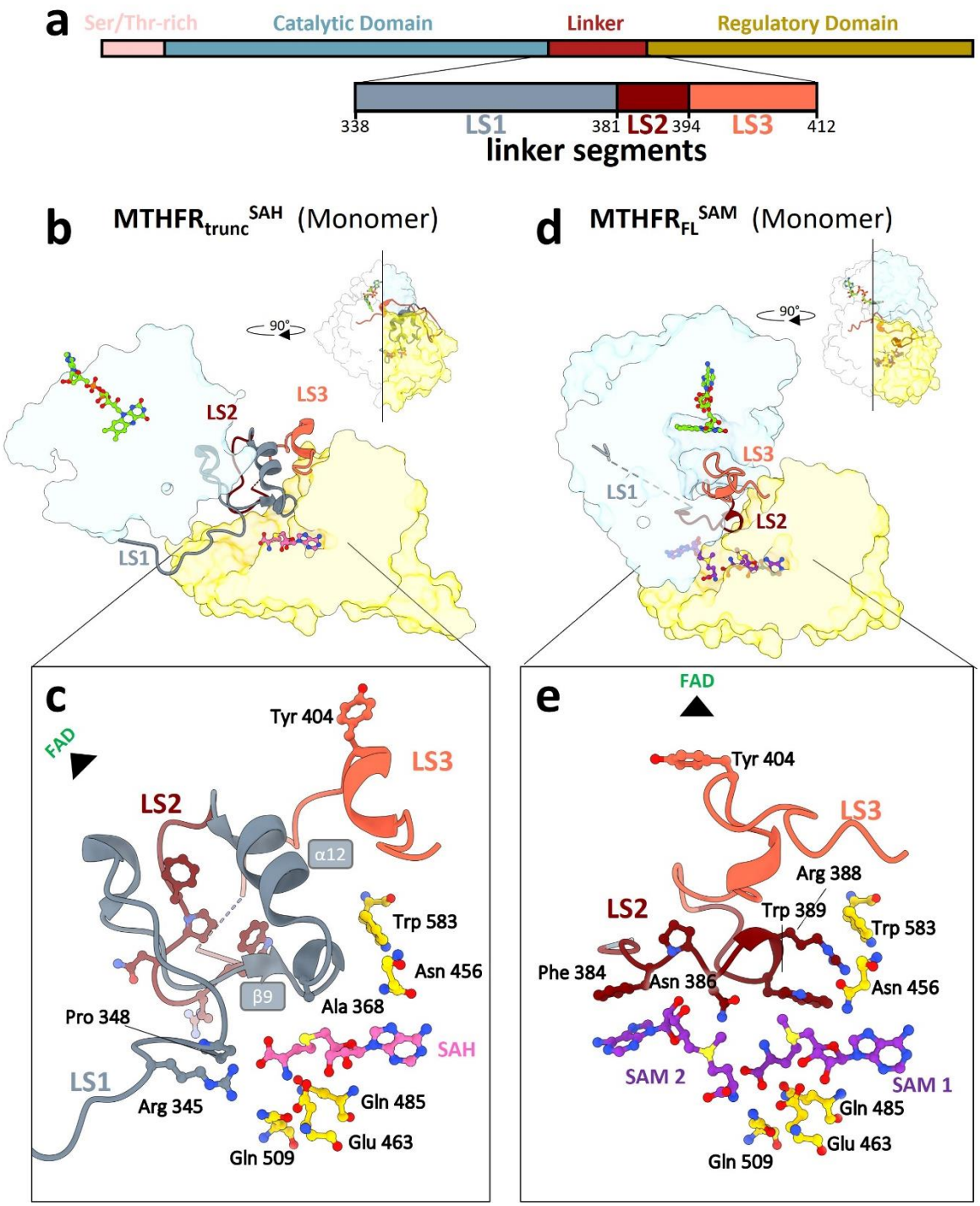

Fig. 3 | Linker reorganisation drives inter-domain reorientation and remodels the allosteric pocket. a, Domain diagram of human $MTHFR_{FL}$, coloured according to MTHFR protein domains and with a zoom-in of linker segments LS1 (aa 338-380), LS2 (aa 381-393) and LS3 (aa 394-412). The colour coding is maintained in subsequent structural representations. **b-e**, Cut-through cartoon representation of monomeric $MTHFR_{trunc}^{SAH}$ (**b**) and $MTHFR_{FL}^{SAM}$ (**d**), showing the extensive rearrangement of LS1, LS2 and LS3. Inserts show a more detailed and zoomed view of the respective allosteric pocket, containing one SAH for $MTHFR_{trunc}^{SAH}$ (**c**) and two SAMs for $MTHFR_{FL}^{SAM}$ (**e**).

Remodelling of the RD pocket switches from binding one SAH to two SAM

The extensive conformational change of the linker region hugely impacts the SAM/SAH binding pocket of the RD. As anticipated, in the $MTHFR_{FL}^{SAM}$ structure, we observed electron density corresponding to one SAM molecule (SAM1) within the RD pocket (referred hereafter as site 1) that was found to accommodate one SAH molecule in $MTHFR_{trunc}^{SAH}$ (Fig. 3c,e and Extended Data Fig. 8a). The same RD residues that interact with SAH are employed in a similar manner to contact SAM1, including for example Glu463 and Thr573 (Extended Data Fig. 8b). However, the charged sulphonium centre enables SAM1 to establish an additional salt bridge with Glu463 (Extended Data Fig. 8b).

Immediately adjacent to SAM1, towards the verge of the RD (referred hereafter as site 2), an unexpected electron density was observed in $MTHFR_{FL}^{SAM}$ (Fig. 3e and Extended Data Fig. 8a). This density feature is not part of any contiguous protein density and initial automatic ligand placement by *Phenix-LigandFit* suggested it to be a second SAM molecule (SAM2). Both SAM1 and SAM2 molecules adopt the same extended configuration with respect to the methionine moiety, and *syn* configuration with respect to the nucleotide-ribose bond (Fig. 3c,e and Extended Data Fig. 8c). SAM1 and SAM2 are juxtaposed in a tail-to-tail manner with their adenosine rings pointing in opposite directions while their methionine moieties face each other (Fig. 3e). This juxtaposition allows hydrogen bonding between the methionyl carboxyl group of SAM1, the methionyl amino group of SAM2, and is further bridged by the strictly invariant residue Gln509 originating from the floor of the binding pocket (Extended Data Fig. 8b).

Our structures therefore reveal that the RD binding pocket undergoes major remodelling to accommodate either one SAH molecule (at site 1) in the dis-inhibited conformer ($MTHFR_{FL}^{SAH}$/$MTHFR_{trunc}^{SAH}$ structures), or two SAM molecules (at sites 1 and 2) in the inhibited conformer ($MTHFR_{FL}^{SAM}$ structure) (Extended Data Fig. 8c). It is also apparent that site 2 is not present in the binding pocket of the dis-inhibited conformer, and only appears upon transition to the inhibited conformer. This switch in ligand binding mode and stoichiometry at the RD pocket is brought about by the substantive rearrangement between the two conformers, directed to the LS1 and LS2 segments of the extended linker region described in the previous section.

More specifically, in the presence of SAH, LS1 loops into the RD pocket to contact the homocysteine and sulphonium moieties, thereby adopting a position that 'seals off' site 2 (Fig. 3c and Extended Data Fig. 8c). Disorder in LS1 in the presence of SAM, by contrast, suggests that upon SAM binding this segment is displaced from the RD pocket to remove the seal. With site 2 open, binding of a second SAM molecule is possible and further stabilised by LS2, which swings from its position at the dimer interface (seen in the $MTHFR_{trunc}^{SAH}$ structure, Extended Data Fig. 7b,c) to the RD binding pocket (seen in the $MTHFR_{FL}^{SAM}$ structure, Fig. 3e and Extended Data Fig. 7d). The highly conserved $F_{384}PNGRW_{389}$ sequence (Supplementary Fig. 2) from LS2 plays a defining role in shaping site 2: Phe384 stacks against the adenosine ring of SAM2 (Fig. 3e and Extended Data Fig. 8b). Likewise, Arg388, Trp389 and Trp583 form a triple π-π stacking interaction in the presence of SAM2 (Fig. 3e).

In addition to contributions from the linker segments, site 2 is further shaped by the rearranged CD-RD orientation. As a result, the $D_{289}NDA_{292}$ sequence between helices α9 and α10 of the CD, which is oriented away from the dimer interface and exposed towards the exterior in the presence of SAH, traverses approximately 40 Å in the presence of SAM to be buried into the interior of the RD and to interact with SAM2 (Extended Data Fig. 7b,d). Asp289, Asp291, and Ala292 all interact with the adenosine group (Extended Data Fig. 8b).

Both SAM binding sites are required for allosteric inhibition

Our structural data point to the unexpected binding of two SAM molecules in the RD pocket of each MTHFR protomer. Prompted by this two-SAM model, we searched for further evidence using biophysical and biochemical approaches. Isothermal titration calorimetry (ITC) of 500 µM SAM or SAH injected into 30 µM as-purified $MTHFR_{FL}$ revealed both ligands to bind the protein in an exothermic reaction, with stronger affinity exhibited by SAH (K_d 0.38-0.39 µM) than SAM (K_d 0.86-0.99 µM) (Fig. 4a and Extended Data Fig. 9a). Importantly, the binding isotherms revealed a binding stoichiometry for SAM (N=1.33) that is double that for SAH (N=0.48) (Fig. 4a and Extended Data Fig. 9a). Consistent with a more extended conformation than in the presence of SAM, SAH binding elicited a greater change in enthalpy as measured by ITC (Extended Data Fig. 8a). Furthermore, the SAM-bound conformer shows a higher melting temperature in DSF measurements (Extended Data Fig. 5f).

The two-SAM model would also imply that binding of both SAM molecules is necessary to elicit allosteric inhibition. To test this, we generated MTHFR variants in three systems: over-expression of variant MTHFR proteins in 293T cells with a genetic *MTHFR* knock-out, genetically engineered 293T cells to endogenously express variant MTHFR proteins and purified recombinant variants of $MTHFR_{FL}$. To examine disruption of SAM1 binding residues we generated the variants Thr573Ala, Thr573Val, Gln485Ala, Gln485Leu and Glu463Gln; for SAM2 binding residues we generated Phe384Ala and Asn386Ala. To assess the importance of the triple π-π stacking interaction towards site 2 we also generated Trp583Ala, Trp389Ala, and Arg388Ala/Glu/Gln. ITC to evaluate binding of SAM to $MTHFR_{FL}$ variant proteins disrupted at site 1 (Glu463Gln) or the π-π stacking interactions (Arg388Gln) revealed no binding event upon injection of SAM to either variant protein (Extended Data Fig. 9b). Indeed, further examination of the enzymatic activity of variants engineered to disrupt the π-π stacking interactions as well as binding to site 1 and site 2 revealed abolished SAM-mediated inhibition in all systems tested (Fig. 4b,c and Extended Data Fig. 10a-j). Therefore, binding of SAM to both site 1 and site 2 is an integral part of this inhibitory process.

The requirement of both sites 1 and 2 further implies that they serve different roles in the inhibitory mechanism, both of which are required and will be achieved only above a certain threshold concentration of SAM (that ensures both sites are occupied). It is therefore tempting to speculate that a single bifunctional ligand, with the capability to engage both sites 1 and 2, could mimic the potency of SAM-mediated inhibition at a potentially lower ligand concentration. We previously identified the SAM derivative (S)-SKI-72 (Fig. 4d) to inhibit MTHFR with a higher potency than SAM itself (IC_{50} 0.8 µM vs 5.8 µM)[18]. We docked (S)-SKI-72 onto the $MTHFR_{FL}^{SAM}$ structure (Fig. 4e, Extended Data Fig. 10k,l, and Supplementary Table 1)[18], showing that the ligand can engage with both sites 1 and 2, while also potentially navigating the space around the CD-RD linker region. Strikingly, the activity of $MTHFR_{FL}$ variants harbouring alanine substitution at residues contributing to binding site 1 (Glu463Gln) or the π-π stacking interactions (Arg388Gln) were inhibited by (S)-SKI-72 to a significantly diminished extent compared to that of wild-type $MTHFR_{FL}$ protein (Fig. 4f). Therefore, our data suggest that (S)-SKI-72 exerts its mode of inhibitory action in a similar manner as SAM, by being able to execute the roles, at least in part, designated for sites 1 and 2.

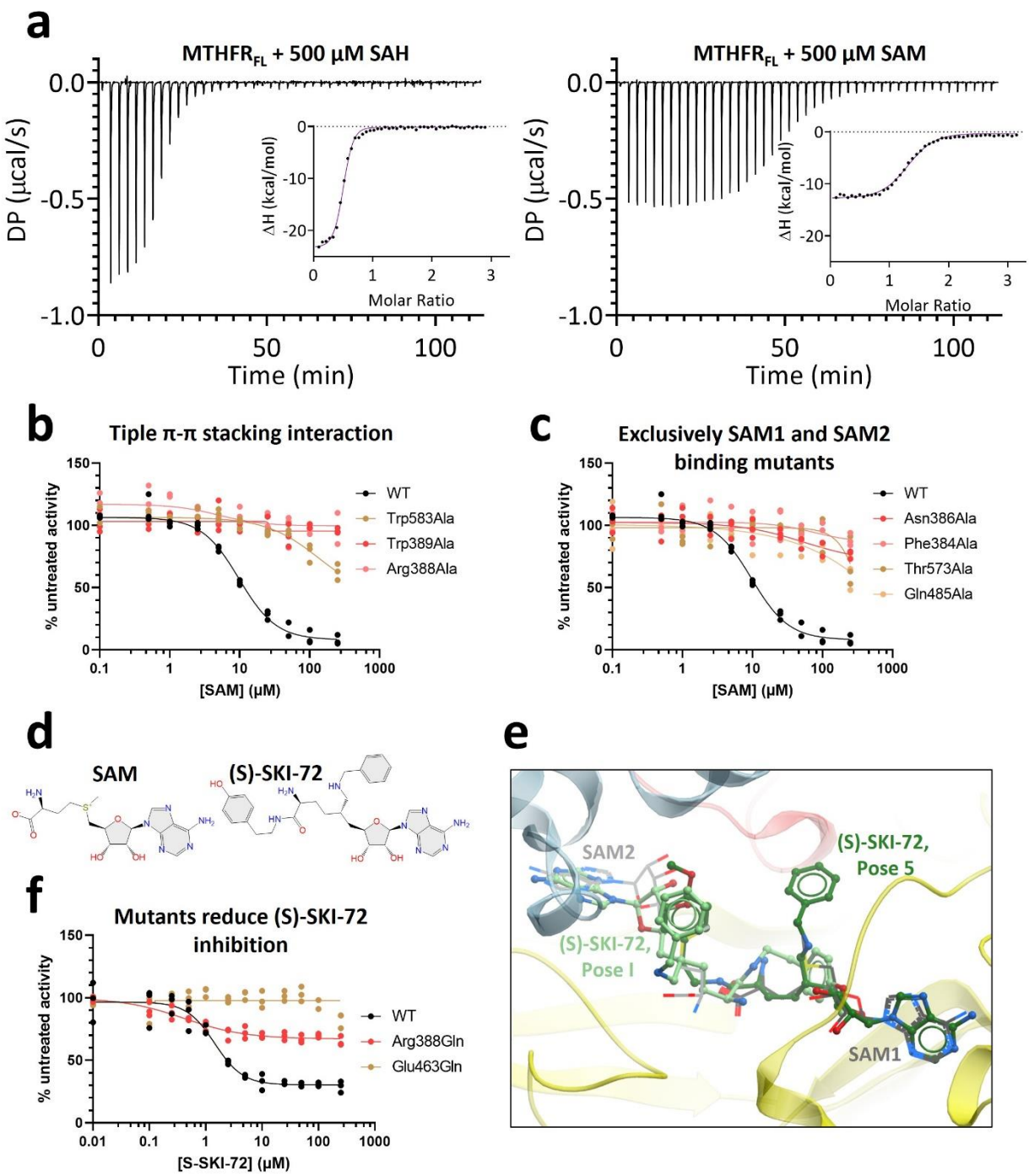

Fig. 4 | Biochemical evidence supporting the two-SAM model. a, Representative ITC experiments displaying the heat exchange over time for the injection of 500 µM SAH or SAM into purified recombinant MTHFR$_{FL}$. DP: power differential. The inset illustrates ΔH (change in enthalpy) plotted against the molar ratio. All curves have been normalized against buffer injected into MTHFR$_{FL}$. N= 2 technical replicates, where the second replicate is shown in Extended Data Fig. 9a. **b-c,** SAM inhibition curves of MTHFR$_{FL}$ and alanine substitutions of residues partaking in triple-π-π stacking interactions (Trp583, Trp389, Arg388) (**b**) or those which exclusively interact with site 2 (Asn386, Phe384), or site 1 (Thr573, Gln485) (**c**). The MTHFR$_{FL}$ variant proteins were overexpressed in HEK293T MTHFR knock-out cells and measured with an HPLC-based activity assay. The WT in **b** and **c** corresponds to the WT seen in Fig. 2e. N=3 biological replicates. Maximum activity for each variant with corresponding Western blots are in Extended Data Fig. 10 and Supplementary Fig. 3. **d**, Chemical structures of SAM and (S)-SKI-72. **e**, Representative docking poses where (S)-SKI-72 adenine group

occupies similar space to that of either SAM1 (Pose 5, dark green) or SAM2 (Pose I, light green) and extends towards the other SAM binding site. SAM molecules are shown as grey lines and (S)-SKI-72 poses are shown as green sticks. All docked poses can be found in Extended Data Fig. 10k,l. Scoring of all poses is presented in Supplementary Table 1. **f**, SAM inhibition curves for recombinant WT as well as Arg388Gln and Glu463Gln $MTHFR_{FL}$ protein incubated with (S)-SKI-72. N=3 technical replicates.

Discussion

When we first reported the crystal structure of human MTHFR, revealing a two-domain architecture with a novel RD fold appended to a conserved CD[16], we captured the enzyme bound with SAH which antagonises the inhibitory action of SAM. That structure adopted a conformation consistent with the role of SAH in dis-inhibiting the enzyme, such that the RD did not crosstalk with the CD. We postulated that crosstalk would occur when SAM binds to the same RD, transmitting a signal to the CD through inter-domain conformational changes. Now, through cryo-EM reconstruction of SAM-bound MTHFR, we have come to realise that the linker is at least 50 aa longer than originally designated, and crucially involved in this regulatory inter-domain crosstalk. Indeed, the direct and indirect participation of the extended linker defines the inhibitory mechanism of MTHFR, in three ways.

Firstly, the linker constitutes the multiplexed signal, transmitted through elaborated conformational gymnastics within its three constituent segments (LS1-LS3). In the presence of SAM, LS1 is displaced from the RD to the exterior, LS2 translocates from the dimer interface to inside the RD, while LS3 moves into the CD. In concert, these movements result in a substantial CD-RD re-orientation, akin to the closing of an oyster shell (Fig. 5a). Decoding this signal further, the LS1 and LS2 movements reshape the RD pocket to bind SAM, and the LS3 movement directly results in active site inhibition. This multiplexed signal now offers the explanation as to why linker residues (particularly LS1 and LS2) directly influence the K_M of NADPH in patients with MTHFR deficiency[27,28] and the sensitivity of SAM inhibition of yeast *met13*[29]. Inspection of MTHFR sequences indicates strong conservation of LS1 between mammals, plants and *C. elegans*, and LS2 (particularly F_{384}PNGRW_{389} motif) across all eukaryotes, pointing to a universal mechanism of the SAM-bound signal transmission for MTHFR.

Secondly, the linker creates an allosteric inhibition mechanism which, in comparison to ligand induced activation mechanisms commonly employed by multi-domain metabolic enzymes, is far more intricate. In well-characterised examples of activation (e.g. CBS[30], PAH[31], DAH7PS[32]), the ground-state enzyme has the access to its active site partially hindered by a juxtaposed regulatory module, resulting in low basal activity; upon binding the activating ligand, this module dimerises and is sequestered away from the active site, allowing maximal activity. MTHFR has clearly evolved a completely different allosteric mechanism in response to an inhibitory (and not activating) ligand, which does not involve a dimerised element. Instead, MTHFR not only juxtaposes LS3 atop the CD, hindering access to the active site (*'block'*), but also plunges its aromatic Y_{403}YLF_{406} motif into the CD, forcing away helix α8 and securely fastening itself to the cofactor FAD within the active site ('*lock*') (Fig. 5b). The complete loss of SAM-mediated inhibition by Tyr404 substitution is a testament to LS3's key role in this block-and-lock strategy.

Interestingly, the LS3 inhibitory sequences, including Y_{403}YLF_{406} (and the CD helix α8 sequences) involved in the human block-and-lock strategy, are not preserved in lower eukaryotes e.g., *S. cerevisiae* MET13 and its homologue MET12[16] We harnessed the predictive power of Alphafold2[33,34] and surveyed the public repertoire of MTHFR models from lower eukaryotes. Strikingly, several models (e.g. *S. cerevisiae* Met12, https://alphafold.ebi.ac.uk/entry/P46151) adopt an inhibited conformation close to our experimental $MTHFR_{FL}{}^{SAM}$ structure, and similarly employ an aromatic (Phe) or hydrophobic (e.g. Ile, Leu) residue to block the NAD(P)H/CH_2-THF binding site. Altogether, we reason that adaptation of the block-and-lock inhibitory strategy for eukaryotic MTHFR was likely an early evolutionary event, although the exact sequence involvement could have diversified in higher eukaryotes.

Thirdly, and perhaps most unexpectedly, the linker directly participates in the creation of a second SAM binding site in the RD (Fig. 5c). Sealed off by LS1 in the SAH-bound dis-inhibited conformer, this second site (site 2) was only observed to be occupied by SAM when the adjacent site (site 1) was also SAM- (and not SAH-) bound. The location of site 2 in the $MTHFR_{FL}^{SAM}$ structure, more exposed to the exterior than site 1, now helps demystify the results of historic photoaffinity labelling studies[12,35] that identified residues in site 2 as important for SAM binding, an observation that puzzled researchers in the field for decades as these residues are some 50 amino acids N-terminal to the then predicted RD. Dual SAM binding has been previously reported for the radical SAM enzyme HemN in *E. coli*[36], where the two SAM ligands have non-equivalent binding sites and likely carry different roles; and *A. thaliana* threonine synthase[37], carrying two symmetrical SAM binding sites. As for MTHFR, the two SAM molecules bound to sites 1 and 2 are non-symmetrical in their ligand conformation and interaction, prompting us to also speculate that SAM1 and SAM2 coordinate different aspects of the inhibitory mechanism.

Since site 2 formation necessitates site 1 to be occupied by SAM and not SAH, we reason that site 1 is tasked with a sensor role, differentiating between the binding of SAM and SAH. The chemical structures of SAM and SAH differ by only a methyl group at the sulphonium centre. When site 1 is occupied by SAH ($MTHFR_{trunc}^{SAH}$ structure[16]), the demethylated sulphonium centre is 3.4-3.6 Å away from Ala368 (within LS1). When SAM1 binds to site 1, adopting an essentially identical ligand configuration to SAH (as shown in $MTHFR_{FL}^{SAM}$), the sulphonium methyl of SAM1 cannot be accommodated by Ala368 were it to retain the dis-inhibited $MTHFR_{trunc}^{SAH}$ conformation. We therefore speculate that the first event upon SAM1 binding is the repositioning of Ala368 to kick-start the LS1 conformational change, consistent with our original attribution of this residue as a SAM sensor[16].

While site 1 may function as a SAM/SAH sensor to trigger the initial process of SAM-mediated inhibition, site 2 likely serves the role of sustaining the inhibition process, further committing the protein to the LS1-LS3 conformational changes. To perform this role, the arrival of SAM2 removes the seal (formed by part of LS1) to site 2 and stabilises the LS2 triple π-π interactions (of Trp389, Arg388 and Trp583) within the RD core. These changes provide the platform of conformational change that ultimately leads to the LS3 block-and-lock. Our proposed dichotomous binding of SAM to the RD is consistent with the very slow (minutes) inhibitory mechanism of SAM[11], and implies a possible 'poised' state of MTHFR that is singly occupied by SAM1, adopting a conformational transition between those captured by the $MTHFR_{trunc}^{SAH}$ and $MTHFR_{FL}^{SAM}$ structures. This putative state has so far evaded experimental entrapment. The existence of other ligand binding states (e.g., site 2 occupied by SAM/SAH with site 1 vacant), while unlikely, also remain to be clarified.

Without doubt, our data beg the question as to why the evolutionary adaption of MTHFR led to the assembly of three advanced modules (dual SAM binding, extensive linker rearrangement, and block-and-lock inhibition) into one metabolic enzyme. We are not aware of any other multi-domain proteins that are constructed in this manner. There are over 18-fold types known to bind SAM[21], and SAM is a well characterised allosteric activator[30] and orthosteric inhibitor[38] of other human proteins. So, what is the imperative for MTHFR to evolve such a unique fold and mechanism, and not merely adapt from a plethora of already existing domains and mechanisms?

Perhaps the answer lies in the critical role that MTHFR plays in one-carbon metabolism, at the juncture of the folate and methionine cycles. MTHFR directly influences the rates of both SAM and pyrimidine biosynthesis in the cell, with important consequences for global trans-methylation and DNA synthesis[39]. To the best of our knowledge, MTHFR is the only human enzyme that is allosterically inhibited by SAM. The opportunity costs are likely

to be so high for both inhibition and dis-inhibition of MTHFR, that a simple 'on/off' regulatory switch trigged by the mere presence/absence of SAM alone is not sufficient for cellular needs. Instead, a multi-layered switch with a built-in sensor that responds to the SAM:SAH ratio allows MTHFR to fine-tune its catalytic response to cellular needs. We propose that with a low SAM:SAH ratio in the cell, MTHFR adopts the dis-inhibited $MTHFR_{trunc}^{SAH}$ state to dedicate one-carbon flux to SAM biosynthesis. When the SAM:SAH equilibrium is tipped towards more SAM, its binding to site 1 primes the enzyme for inhibition. At a high SAM:SAH ratio, the excess SAM in the cell ensures subsequent binding of SAM to site 2, thereby triggering the cascade of events eventually leading to a fully inhibited protein (as seen in $MTHFR_{FL}^{SAM}$) and thereby a biological commitment to switch-off SAM biosynthesis.

This depiction, however, is still likely an over-simplification. MTHFR functions as a homodimer, where the two constituent protomers function essentially independently, and could therefore adopt different binding states. Considering this, a continuum of SAM-bound, SAH-bound and unliganded states of an MTHFR homodimer would more closely reflect the physiological scenario in the cell, in line with our previous observation of multiple MTHFR conformations from SAXS[16]. This is further coupled to the additional regulation mediated by Ser/Thr phosphorylation at the N-terminus of the enzyme. We have previously shown that this phosphorylation sensitises SAM inhibition by lowering its K_i[16]. Thus, it is likely that phosphorylation primes either SAM binding or the consequent conformational change. To do so, the N-terminal region would likely have to interact with one (or more) of the linker segments. In the $MTHFR_{FL}^{SAM}$ homodimer, LS1 from each protomer is disordered but would be exposed to the same face of the protomer as would the N-terminus, at the dimer interface. Despite the presence and likely phosphorylation of the N-terminal region in $MTHFR_{FL}$, it could not be resolved in our cryo-EM reconstruction due to intrinsic disorder. Therefore, future structural studies will be needed to clarify how the (de)phosphorylated N-terminus interacts with the rest of MTHFR and primes inhibition.

Beyond shedding new light into the inhibitory mechanism, this study also illuminates distinctive strategies for the development of MTHFR inhibitors and activators, which could have a diverse set of therapeutic indications. Human MTHFR is a highly attractive target as one could minimise the risk of cross-reactivity by exploiting its unique fold within the human proteome. We envisage that small molecules targeting the $MTHFR_{FL}^{SAH}$ conformer, through binding to site 1, could be a therapeutic avenue for MTHFR deficiency where the residual enzyme could be dis-inhibited. On the contrary, compounds like (S)-SKI-72[18], which are potentially capable of fulfilling both SAM1 and SAM2 roles at the RD, could be developed as potent inhibitors, addressing disease states exhibiting MTHFR overexpression or hyperactivity that need to be down-regulated (e.g. cancer).

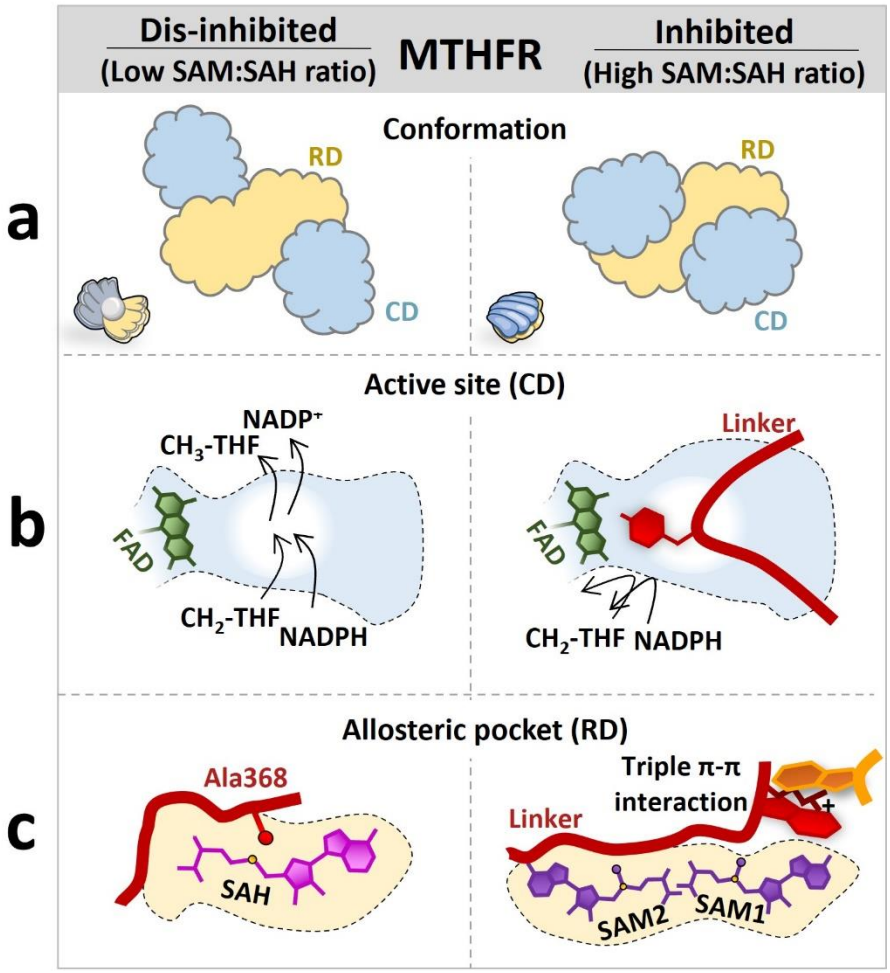

Fig. 5 | Schematics summarising the allosteric regulation of MTHFR. Each panel provides an overview of the **a**, conformation **b**, active site and **c**, allosteric pocket of dis-inhibited (left) and inhibited (right) MTHFR. Left, in the presence of a low SAM:SAH ratio, MTHFR is in an open conformation (like an open oyster), with free access to its active site and with only one SAH bound in its allosteric pocket. Right, in the presence of a high SAM:SAH ratio, MTHFR is in its closed conformation (like a closed oyster) with the linker blocking the access to the active site, and two SAM molecules bound within the allosteric pocket.

Table. 1 | Cryo-EM data collection, refinement, and validation statistics.

	MTHFR + SAH symmetric dis-inhibited state (EMDB-18298) (PDB 8QA4)	MTHFR + SAH asymmetric dis-inhibited state (EMDB-18299) (PDB 8QA5)	MTHFR + SAM, inhibited state (EMDB-18300) (PDB 8QA6)
Data collection and processing			
Magnification	240,000		240,000
Voltage (kV)	200		200
Electron exposure (e^{-}/Å^2)	50		50
Defocus range (μm)	-0.9 to -2.1		-0.9 to -2.1
Pixel size (Å)	0.574		0.574
Symmetry imposed	C2	C1	C2
Initial particle images (no.)	1,980,846	1,980,846	882,089
Final particle images (no.)	105,879	104,101	135,192
Map resolution (Å)	2.8	3.1	2.9
FSC threshold	0.143	0.143	0.143
Map resolution range (Å)	2.0-4.5	2.5-7.5	2.7-5.8
Refinement			
Initial model used (PDB code)	6FCX	6FCX	AlphaFold/ SwissProt
Model resolution (Å)	3.0	3.5	3.2
FSC threshold	0.5	0.5	0.5
Map sharpening *B* factor (Å^2)	-90.1	-86.3	-105.2
Model composition			
Non-hydrogen atoms	3820	5569	9088
Protein residues	462	814	1106
Ligands	SAH (2)	FAD (1), SAH (2)	FAD (2), SAM (4)
B factors (Å^2)			
Protein	29.71	92.83	84.20
Ligand	29.54	224.13	80.55
R.m.s. deviations			
Bond lengths (Å)	0.023	0.027	0.022
Bond angles (°)	2.298	2.318	1.531
Validation			
MolProbity score	1.50	1.48	1.59
Clashscore	3.62	2.37	6.69
Poor rotamers (%)	1.45	1.48	0.52
Ramachandran plot			
Favored (%)	96.49	95.14	96.62
Allowed (%)	3.51	4.74	3.38
Disallowed (%)	0.0	0.12	0.0

Methods

Cloning, expression, and purification

Cloning, expression, and purification of human full-length $MTHFR_{FL}$ wild-type and variants were generated as previously described for purified recombinant[16], overexpressed-[28,40] and endogenously expressed[18] MTHFR. In brief, pure recombinant $MTHFR_{FL}$ with a C-terminal flag/His_{10} tag and variants generate with site-directed mutagenesis, were expressed in SF9 cells and purified by affinity (Ni-NTA, Qiagen) followed by size exclusion (Superdex 200) chromatography. Purified MTHFR was concentrated to 10–15 mg ml^{-1} and stored at −80 °C in storage buffer (50 mM HEPES pH 7.5, 500 mM NaCl, 5% glycerol, 0.5 mM TCEP). Overexpressed $MTHFR_{FL}$ with C-terminal flag/His_{10}-tag encoded in a pcDNA3-CT10HF-LIC backbone and variants generated with site-directed mutagenesis, were transfected using Lipofectamine 3000 (Invitrogen, 15292465) into 70-90% confluent HEK293T MTHFR knock-out cells. The cells were incubated at 37 °C for 72 h before harvested and snap frozen. Expression was confirmed by western blot. Endogenously $MTHFR_{FL}$ and variants, were generated though homology-directed repair by mixing HEK293T cells with Cas9 vector (Invitrogen, TrueCut Cas9 Protein v2, A36496), gRNA and ssODN template before treated with two pulses of 1150 V for 20 ms in a Neon transfection system (Invitrogen, MPK5000), followed by 48 h incubation before single cell seeded. All gRNA and ssODN can be found in Supplementary Table 2. The CRISPR/Cas9-edited mutants were validated by DNA extraction using QuickExtract solution (Lucigen, QER090150) followed by sanger sequencing prior cell line expansion[28,38]. Site-directed mutagenesis was performed using Phusion High-Fidelity DNA Polymerase (New England Biolabs). All primer sequences can be found in Supplementary Table 3. Overexpressed and endogenously $MTHFR_{FL}$ and variants were lysed by 30 min incubation with ice-cold lysis buffer (0.01 M K2HPO4-buffer pH 6.6 with 0.15% luberol). To prepare purified recombinant MTHFR for negative stain and cryo-EM imaging experiments, the flag/His_{10}-tag was removed by overnight incubation at 4°C with His-tagged tobacco etch virus protease followed by multiple washes on Ni-NTA loaded resin column, as previously described[40,41].

Negative stain EM

TEV-cleaved purified recombinant $MTHFR_{FL}$ was diluted to a final concentration of 50 nM in buffer (20 mM HEPES pH 7.5, 200 mM NaCl) containing 5 mM SAM or 2.6 mM SAH. 3 µl sample was added to S160-3 Carbon Film 300 Mesh Cu (25) (Agar Scientific) grids, plasma treated using PELCO easiGlow™ (Ted Pella, Inc). The grids were blotted by hand, washed in ultra-pure water before stained using 2% (w/v) uranyl acetate. Imaging of the stained grids was performed using a Hitachi HT7800 microscope operating at 120 kV, located at the Electron Microscopy Research Services (EMRS) facility at Newcastle University. Images were captured on a Hitachi HT7800, at defocus with a magnification of 70K and a pixel size of 1.8 Å. cryoSPARC-v4.2.1[42] was used for processing of micrographs.

Cryo-EM sample preparation and data acquisition

All grids were glow discharged using PELCO easiGlow™ (Ted Pella, Inc) and blotted using Vitrobot (Thermo Scientific) using temperature 4 °C and 100% humidity for Quantifoil Au R1.2/1.3, 300 mesh grids and at 22 °C and 100% humidity for Au-Flat or UltrAuFoil R1.2/1.3, 300 mesh grids. For active $MTHFR_{FL}^{SAH}$, TEV-cleaved purified recombinant $MTHFR_{FL}$ was diluted to 2 mg/ml in EM-buffer 1 (20 mM HEPES, pH 7.5, 150 mM NaCl, 0.0025% Tween20) with 1 mM SAH or diluted to 1 mg/ml in EM-buffer 2 (20 mM HEPES, pH 7.5, 150 mM NaCl) with 1 mM SAH. For $MTHFR_{FL}^{SAM}$, TEV-cleaved purified recombinant $MTHFR_{FL}$ was

diluted to 2 mg/ml in either cryo-EM buffer 2 or buffer 3 (10 mM Potassium-Phosphate, pH 6.6) with 5 mM SAM. All data collections were done at the York Structural Biology Laboratory (YSBL) on a Glacios equipped with a Falcon 4 direct electron detector (Thermo Fisher Scientific). EER formatted movies were imaged at 200 kV with a magnification of 240k, with a pixel size of 0.574 Å. Movies over 5.18 seconds were recorded with a defocus range of –0.9 µm to –2.1 µm with a total dose of 50 $e^{-}A^{2}$. For $MTHFR_{FL}^{SAH}$ in total 5606 micrographs were collected and pooled from two different grids. For $MTHFR_{FL}^{SAM}$ in total 2394 micrographs were collected and pooled from three different grids. The two data sets were collected at two separate sessions. For further details see Extended Data Figs. 2a and 3a.

All datasets were imported into cryoSPARC-v4.2.1[42] and were subjected to patch motion and patch CTF correction. For more detailed information on the processing workflow for all datasets please see extended data figures 2 and 3. To determine the asymmetric SAH-bound state, particles from a C2 local refinement of the regulatory domain dimer were subjected to symmetry expansion. This was then followed by 3D classification in CryoSPARC to classify the heterogeneity of the flexible catalytic domains while maintaining the angles from the C2 symmetry applied local refinement, like symmetry relaxation as implemented in Relion[43]. Two sets of classes were determined representing the CD being less flexible for one protomer and absent for the other. One set of these classes were pooled and then subjected to a local refinement without symmetry applied. This used a soft mask that encompassed both the central RD dimer along with a single, less flexible, catalytic domain. The resulting map was then locally sharpened in CryoSPARC to aid in interpretability. Overall, our data collections resulted in a map of the central RD dimer bound to SAH at 2.8 Å, an asymmetric map of the SAH-bound state at 3.1 Å, and a map of the SAM-bound state at 2.9 Å.

Model fitting, refinement, and validation.

For both $MTHFR_{FL}^{SAH}$ structures, the crystal structure $MTHFR_{trunc}$ (PDB 6FCX) was used as an initial model and rigid docked into both maps in ChimeraX[44]. Regions not represented in the density were appropriately deleted. For the flexible CD, sidechains were truncated to alanine. For the $MTHFR_{FL}^{SAM}$ structure a homology model was created using SWISS-MODEL[45] and the AlphaFold[33,34] predicted structure of Met12 which appeared to be in an inhibited conformation and presented features like the $MTHFR_{FL}^{SAM}$ map. This homology model was docked into the density using ChimeraX[44] and regions of the model not represented by the density were deleted. SAM and FAD ligands were initially fitted using LigandFit in Phenix[46]. For refinement of all models Namdinator[47] was used for flexible fitting followed by iterative rounds of ISOLDE[48], manual adjustment in COOT[49], and Phenix real space refinement[50]. Models were validated using MolProbity[51], model fit was assessed using the Q-score[52] implementation in ChimeraX[44], which was also used to create figures.

HPLC activity assay.

All enzymatic assays were performed with an HPLC-based physiological forward assay for MTHFR originally described by Suormal et al.[41] with adaptations for measurements in lysate from overexpression in HEK293T MTHFR knock-out cells or endogenous in genetically modified HEK293T[27,28] , and in purified recombinant protein[16]. All enzymatic reactions were performed in 96-well plates and scaled down to reaction volumes of 20-50 µl. For ligand inhibition assay, the reaction mixtures were preincubated for 5 min at 37°C with purified SAM[53], with SAH (Sigma-Aldrich, A9384) or (S)-SKI-72[18] prior to reaction initiation. Curve fit was preformed using inhibitor versus response [four-parameter curve fit] by GraphPad Prism (v9). Untreated specific activity was obtained from samples with no ligand addition.

Isothermal titration calorimetry

Purified $MTHFR_{FL}$ and variants were buffer exchanged using Zebra spin desalting columns (Thermo Scientific) using filtrated (0.2 µm) 25 mM HEPES buffer, with ligands diluted in the very same buffer. An ITC 200 microcalorimeter (Malvern Instruments, Malvern, UK) was used for all measurements, titrating ligand (500 µM SAM or 500 µM SAH) into the calorimetric cell containing MTHFR protein at approximately 30.0 µM or 10.0 µM. For runs of 45 injections, 0.8 µl injections were used, for 19 injections, 3 µl injection volumes were used. In both sets of experiments injections were spaced with 150s intervals and ran at 25°C. The resulting isotherms were subtracted against ligand titrated into buffer only runs and the data evaluated using MicroCal PEAQ-ITC software (Malvern Instruments).

Differential scanning fluorimetry

The binding events between SAM or SAH and $MTHFR_{FL}$ variants were detected either by the emitted fluorescence from a fluorometric dye or by detecting the emission from FAD. The samples were prepared in 96-well PCR plates, where each well (20 µl) contained 0.1 mg/ml purified recombinant protein, buffer (10 mM HEPES pH 7.5, 500 mM NaCl) and 1 mM SAM, 1 mM SAH or no ligand. The samples were incubated for 10 minutes at room temperature before the addition of SYPRO-Orange dye (#S6650, Invitrogen) diluted 500X or water for FAD emission. All fluorescence measurements were performed using QuantStudio 5 (Applied Biosystems), with SYBR set as the reporter, and a temperature ramp of 0.05°C/s from 25 to 99°C. Raw data are available in Supplementary Fig. 1.

Western Blotting

Western blotting analysis was performed using as primary antibody 1:2000 diluted monoclonal mouse anti-flag (Sigma, F3165) to target MTHFR or 1:5000 diluted monoclonal mouse anti-ACTB (sigma, A1978) as loading control, and as secondary antibody 1:5000 diluted mouse IgG kappa binding protein conjugated to Horseradish Peroxidase (Santa Cruz, sc-516102). Nitrocellulose membranes (Cytiva, 10600007) were developed using enhanced chemiluminescence detection reagents (Cytiva, Amersham ECL Western Blotting Analysis System, RPN2109) and imaged with a ChemiDoc Touch Imaging System (Bio-Rad). Uncropped images are available in Supplementary Fig. 3.

Docking of (S)-SKI-72

Docking was performed in ICM-Pro software (Molsoft LLC). To prepare the docking receptor, the $MTHFR_{FL}^{SAM}$ structure solved in this work was converted to an ICM object. After global energy minimisation, each protein chain was split into a separate object and SAM was removed from the model to clear the pocket. Next, receptor maps were made using the ICM interactive docking function, with the binding pocket defined as a box of 28 x 28 x 42 Å, centred around both SAM molecules. (S)-SKI-72 was then converted to 3D, minimised and its adenine group was superimposed with the adenine group of either SAM1 or SAM2, as the starting position from which docking was performed. From each position, (S)-SKI-72 was docked into the prepared receptor, using ICM interactive docking function to retain the top 5 scoring binding poses (poses 1 – 5 from SAM1 starting point and poses I – V from SAM2 starting point). Poses were ranked according to three separate scoring functions: ICM-VLS score (a combined metric incorporating van der Waals interaction energy, number of torsions in the ligand, the solvation electrostatics energy change upon binding, the hydrogen bond energy, hydrophobic energy in exposing a surface to water, and the desolvation of exposed H-bond donors and acceptors); RT-CNN score (Radial Convolutional Neural Net including layers that do Topological (chemical graph) convolutions and 3D Radial convolutions; a neural network trained to

recognize native-like complexes versus decoys directly, based only on geometries of putative complexes); and LE score (ICM-VLS score weighted to account for ligand strain).

Data availability

Structures and EM maps of MTHFR + SAH symmetric dis-inhibited state (EMDB-18298, PDB 8QA4), MTHFR + SAH asymmetric dis-inhibited state (EMDB-18299, PDB-8QA5), and MTHFR + SAM, inhibited state (EMDB-18300, PDB-8QA6) have been deposited to the EMDB and PDB databases. All main data supporting the findings of this study are available within the article, Extended Data, and Supplementary Information. Source data are provided with this paper.

References

1. Petrossian, T. C. & Clarke, S. G. Uncovering the human methyltransferasome. *Mol Cell Proteomics* **10**, (2011).
2. Lu, S. C. S-Adenosylmethionine. *Int J Biochem Cell Biol* **32**, 391–395 (2000).
3. Igari, S. *et al.* Properties and crystal structure of methylenetetrahydrofolate reductase from Thermus thermophilus HB8. *PLoS One* **6**, (2011).
4. Liew, S. C. & Gupta, E. Das. Methylenetetrahydrofolate reductase (MTHFR) C677T polymorphism: Epidemiology, metabolism and the associated diseases. *Eur J Med Genet* **58**, 1–10 (2015).
5. Izmirli, M. A literature review of MTHFR (C677T and A1298C polymorphisms) and cancer risk. *Molecular Biology Reports 2012 40:1* **40**, 625–637 (2012).
6. Frosst, P. *et al.* A candidate genetic risk factor for vascular disease: a common mutation in methylenetetrahydrofolate reductase. *Nature Genetics 1995 10:1* **10**, 111–113 (1995).
7. Raghubeer, S., Matsha, T. E., Mccaddon, A. & Miller, J. W. Methylenetetrahydrofolate (MTHFR), the One-Carbon Cycle, and Cardiovascular Risks. *Nutrients 2021, Vol. 13, Page 4562* **13**, 4562 (2021).
8. Parle-McDermott, A. *et al.* Analysis of the MTHFR 1298A→C and 677C→T polymorphisms as risk factors for neural tube defects. *Journal of Human Genetics 2003 48:4* **48**, 190–193 (2003).
9. Kirke, P. N. *et al.* Impact of the MTHFR C677T polymorphism on risk of neural tube defects: case-control study. *BMJ* **328**, 1535–1536 (2004).
10. Froese, D. S. *et al.* Mutation update and review of severe methylenetetrahydrofolate reductase deficiency. *Hum. Mutat.* **37**, 427–438 (2016).
11. Kutzbach, C. & Stokstad, E. L. R. Mammalian methylenetetrahydrofolate reductase. Partial purification, properties, and inhibition by S-adenosylmethionine. *Biochim Biophys Acta* **250**, 459–477 (1971).
12. Sumner, J., Jencks, D. A., Khani, S. & Matthews, R. G. Photoaffinity labeling of methylenetetrahydrofolate reductase with 8-azido-S-adenosylmethionine. *Journal of Biological Chemistry* **261**, 7697–7700 (1986).
13. Daubner, S. C. & Matthews, R. G. Purification and properties of methylenetetrahydrofolate reductase from pig liver. *Journal of Biological Chemistry* **257**, 140–145 (1982).
14. Yamada, K., Chen, Z., Rozen, R. & Matthews, R. G. Effects of common polymorphisms on the properties of recombinant human methylenetetrahydrofolate reductase. *Proc Natl Acad Sci U S A* **98**, 14853–14858 (2001).

15. Yamada, K., Strahler, J. R., Andrews, P. C. & Matthews, R. G. Regulation of human methylenetetrahydrofolate reductase by phosphorylation. *Proc Natl Acad Sci U S A* **102**, 10454–10459 (2005).
16. Froese, D. S. *et al.* Structural basis for the regulation of human 5,10-methylenetetrahydrofolate reductase by phosphorylation and S-adenosylmethionine inhibition. *Nature Communications 2018 9:1* **9**, 1–13 (2018).
17. Matthews, R. G., Vanon, M. A., Hainfeld, J. F. & Wall, J. Methylenetetrahydrofolate reductase. Evidence for spatially distinct subunit domains obtained by scanning transmission electron microscopy and limited proteolysis. *Journal of Biological Chemistry* **259**, 11647–11650 (1984).
18. Bezerra, G. A. *et al.* Identification of small molecule allosteric modulators of 5,10-methylenetetrahydrofolate reductase (MTHFR) by targeting its unique regulatory domain. *Biochimie* **183**, 100–107 (2021).
19. Guenther, B. D. *et al.* The structure and properties of methylenetetrahydrofolate reductase from Escherichia coli suggest how folate ameliorates human hyperhomocysteinemia. *Nat Struct Biol* **6**, 359–365 (1999).
20. Pejchal, R. *et al.* Structural perturbations in the Ala → Val polymorphism of methylenetetrahydrofolate reductase: How binding of folates may protect against inactivation. *Biochemistry* **45**, 4808–4818 (2006).
21. Gana, R., Rao, S., Huang, H., Wu, C. & Vasudevan, S. Structural and functional studies of S-adenosyl-L-methionine binding proteins: a ligand-centric approach. *BMC Struct Biol* **13**, (2013).
22. Lee, M. N. *et al.* A Functional Role for the Conformationally Mobile Phenylalanine 223 in the Reaction of Methylenetetrahydrofolate Reductase from E. coli. *Biochemistry* **48**, 7673 (2009).
23. Greber, B. J., Remis, J., Ali, S. & Nogales, E. 2.5 Å-resolution structure of human CDK-activating kinase bound to the clinical inhibitor ICEC0942. *Biophys J* **120**, 677–686 (2021).
24. Pejchal, R., Sargeant, R. & Ludwig, M. L. Structures of NADH and CH3-H4folate complexes of Escherichia coli methylenetetrahydrofolate reductase reveal a Spartan strategy for a ping-pong reaction. *Biochemistry* **44**, 11447–11457 (2005).
25. Trimmer, E. E., Ballou, D. P. & Matthews, R. G. Methylenetetrahydrofolate reductase from escherichia coli: Elucidation of the kinetic mechanism by steady-state and rapid-reaction studies. *Biochemistry* **40**, 6205–6215 (2001).
26. Sheppard, C. A., Trimmer, E. E. & Matthews, R. G. Purification and properties of NADH-dependent 5,10- methylenetetrahydrofolate reductase (MetF) from Escherichia coli. *J Bacteriol* **181**, 718–725 (1999).
27. Burda, P. *et al.* Insights into Severe 5,10-Methylenetetrahydrofolate Reductase Deficiency: Molecular Genetic and Enzymatic Characterization of 76 Patients. *Hum Mutat* **36**, 611–621 (2015).
28. Burda, P. *et al.* Functional characterization of missense mutations in severe methylenetetrahydrofolate reductase deficiency using a human expression system. *J Inherit Metab Dis* **40**, 297–306 (2017).
29. Bhatia, M. *et al.* Allosteric inhibition of MTHFR prevents futile SAM cycling and maintains nucleotide pools in one-carbon metabolism. *Journal of Biological Chemistry* **295**, 16037–16057 (2020).
30. McCorvie, T. J. *et al.* Inter-domain Communication of Human Cystathionine β-Synthase. *Journal of Biological Chemistry* **289**, 36018–36030 (2014).

31. Patel, D., Kopec, J., Fitzpatrick, F., Mccorvie, T. J. & Yue, W. W. Structural basis for ligand-dependent dimerization of phenylalanine hydroxylase regulatory domain. *Scientific Reports 2016 6:1* **6**, 1–10 (2016).
32. Jiao, W., Lang, E. J., Bai, Y., Fan, Y. & Parker, E. J. Diverse allosteric componentry and mechanisms control entry into aromatic metabolite biosynthesis. *Curr Opin Struct Biol* **65**, 159–167 (2020).
33. Jumper, J. *et al.* Highly accurate protein structure prediction with AlphaFold. *Nature 2021 596:7873* **596**, 583–589 (2021).
34. Varadi, M. *et al.* AlphaFold Protein Structure Database: massively expanding the structural coverage of protein-sequence space with high-accuracy models. *Nucleic Acids Res* **50**, D439–D444 (2022).
35. Goyette, P. *et al.* Human methylenetetrahydrofolate reductase: isolation of cDNA, mapping and mutation identification. *Nat Genet* **7**, 195–200 (1994).
36. Layer, G., Moser, J., Heinz, D. W., Jahn, D. & Schubert, W. D. Crystal structure of coproporphyrinogen III oxidase reveals cofactor geometry of Radical SAM enzymes. *EMBO J* **22**, 6214–6224 (2003).
37. Mas-Droux, C., Biou, V. & Dumas, R. Allosteric threonine synthase: Reorganization of the pyridoxal phosphate site upon asymmetric activation through S-adenosylmethionine binding to a novel site. *Journal of Biological Chemistry* **281**, 5188–5196 (2006).
38. LeGros, H. L., Halim, A. B., Geller, A. M. & Kotb, M. Cloning, expression, and functional characterization of the β regulatory subunit of human methionine adenosyltransferase (MAT II). *Journal of Biological Chemistry* **275**, 2359–2366 (2000).
39. Raghubeer, S., Matsha, T. E., Mccaddon, A. & Miller, J. W. Methylenetetrahydrofolate (MTHFR), the One-Carbon Cycle, and Cardiovascular Risks. *Nutrients 2021, Vol. 13, Page 4562* **13**, 4562 (2021).
40. Weile, J. *et al.* Shifting landscapes of human MTHFR missense-variant effects. (2021) doi:10.1016/j.ajhg.2021.05.009.
41. Suormala, T., Gamse, G. & Fowler, B. 5,10-Methylenetetrahydrofolate Reductase (MTHFR) Assay in the Forward Direction: Residual Activity in MTHFR Deficiency. *Clin Chem* **48**, 835–843 (2002).
42. Punjani, A., Rubinstein, J. L., Fleet, D. J. & Brubaker, M. A. cryoSPARC: algorithms for rapid unsupervised cryo-EM structure determination. *Nature Methods 2017 14:3* **14**, 290–296 (2017).
43. Huiskonen, J. T. Image processing for cryogenic transmission electron microscopy of symmetry-mismatched complexes. *Biosci Rep* **38**, 20170203 (2018).
44. Pettersen, E. F. *et al.* UCSF ChimeraX: Structure visualization for researchers, educators, and developers. *Protein Sci* **30**, 70–82 (2021).
45. Waterhouse, A. *et al.* SWISS-MODEL: homology modelling of protein structures and complexes. *Nucleic Acids Res* **46**, W296–W303 (2018).
46. Liebschner, D. *et al.* Macromolecular structure determination using X-rays, neutrons and electrons: recent developments in Phenix. *Acta Crystallogr D Struct Biol* **75**, 861–877 (2019).
47. Kidmose, R. T. *et al.* Namdinator - automatic molecular dynamics flexible fitting of structural models into cryo-EM and crystallography experimental maps. *IUCrJ* **6**, 526–531 (2019).
48. Croll, T. I. ISOLDE: a physically realistic environment for model building into low-resolution electron-density maps. *Acta Crystallogr D Struct Biol* **74**, 519–530 (2018).

49. Emsley, P. & Cowtan, K. Coot: model-building tools for molecular graphics. *Acta Crystallogr D Biol Crystallogr* **60**, 2126–2132 (2004).
50. Afonine, P. V. *et al.* Real-space refinement in PHENIX for cryo-EM and crystallography. *Acta Crystallogr D Struct Biol* **74**, 531–544 (2018).
51. Chen, V. B. *et al.* MolProbity: all-atom structure validation for macromolecular crystallography. *Acta Crystallogr D Biol Crystallogr* **66**, 12–21 (2010).
52. Pintilie, G. *et al.* Measurement of atom resolvability in cryo-EM maps with Q-scores. *Nature Methods 2020 17:3* **17**, 328–334 (2020).
53. Shapiro, S. K. & Ehninger, D. J. Methods for the analysis and preparation of adenosylmethionine and adenosylhomocysteine. *Anal Biochem* **15**, 323–333 (1966).
54. Hayward, S. & Berendsen, H. J. C. Systematic Analysis of Domain Motions in Proteins From Conformational Change: New Results on Citrate Synthase and T4 Lysozyme. *Proteins* **30**, 144–154 (1998).
55. Adasme, M. F. *et al.* PLIP 2021: expanding the scope of the protein-ligand interaction profiler to DNA and RNA. *Nucleic Acids Res* **49**, W530–W534 (2021).

Acknowledgements

We thank Nicola Burgess-Brown and Eleanor Williams from Centre for Medicines Discovery University of Oxford, for the generous gift of the MTHFR expressing constructs. Negative stain electron microscopy was done at Newcastle University EM Research Services, and we are grateful to Tracey Davey for technical support. The Newcastle University EM Research Services is funded by the BBSRC (grant number BB/R013942/1). We thank Johan Turkenburg and Sam Hart for their assistance in collecting Glacios data at York Structural Biology Laboratory (YSBL). The YSBL is funded by the BBSRC, the Wellcome Trust (grant number 206161/Z/17/Z), Tony Wild, and the Wolfson Foundation. D.S.F is supported by the Swiss National Science Foundation [310030_192505] and the University Research Priority Program of the University of Zurich ITINERARE – Innovative Therapies in Rare Diseases. L.K.M.B. was supported by the Children's Research Center Wifor Fellowship of the University Children's Hospital Zurich. W.W.Y. holds a visiting professorship at Nuffield Department of Medicine, University of Oxford.

Author contributions

L.K.M.B., W.W.Y., D.S.F., and T.J.M. designed the experiments. L.K.M.B. performed protein expression and purification, collected EM data, analyzed, and refined all MTHFR structures, along with the ITC, DSF, western blot, and activity assays. M.H. performed site-directed mutagenesis, protein over-expression, western blot, activity assays and assisted in CRISPR/Cas9 work. S.R.M. carried out *in silico* docking. C.B. designed and created CRISPR/Cas9 modified 293T cell lines. A.B. assisted in initial EM processing. T.J.M. assisted in screening, collecting, and processing EM data, along with ITC experiments. L.K.M.B., W.W.Y., D.S.F., and T.J.M. analyzed the data and wrote the manuscript with contributions from all authors. W.W.Y., D.S.F., and T.J.M. supervised the project. W.W.Y. and D.S.F. conceived the project and procured funding.

Competing interests

All authors declare no competing interests.

Correspondence and requests for materials should be addressed to Wyatt W. Yue, D. Sean Froese, or Thomas J. McCorvie

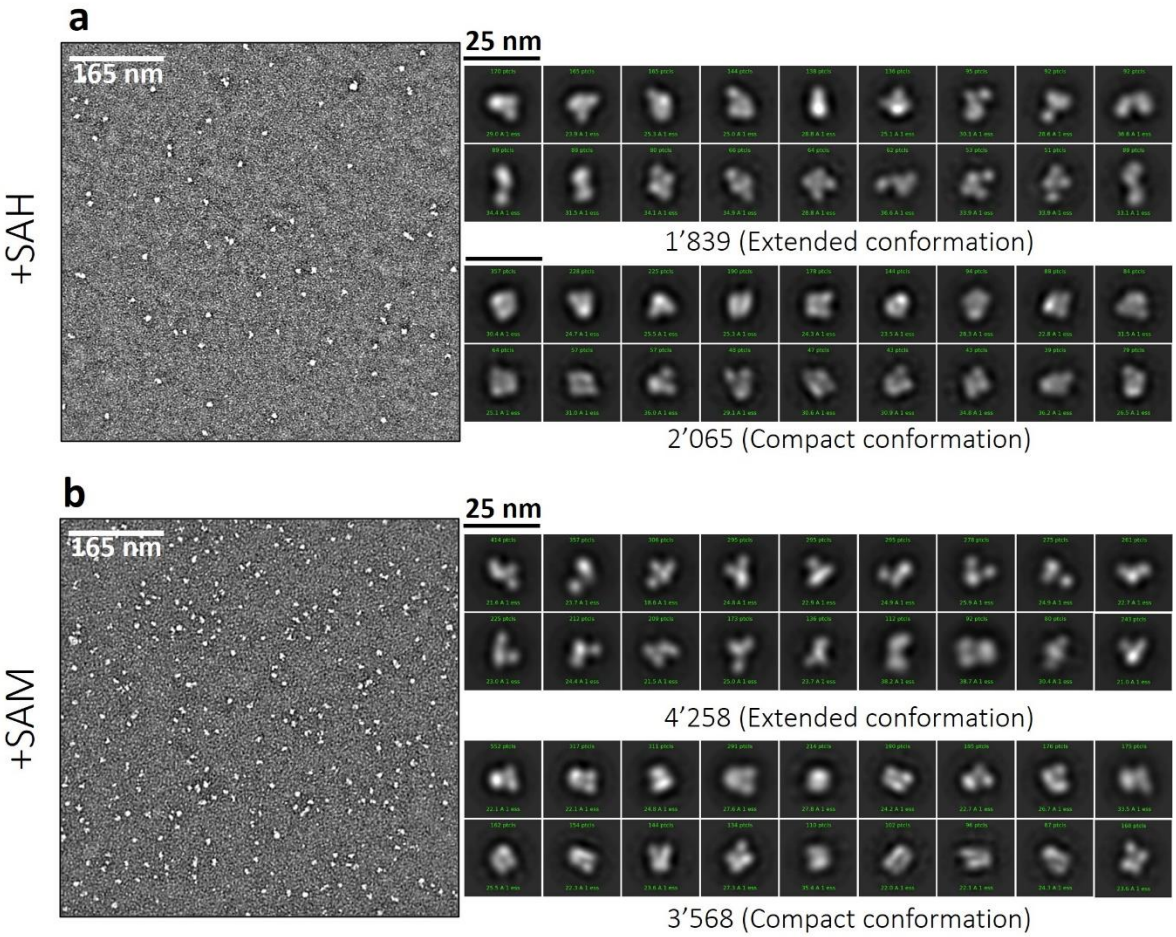

Extended Data Fig. 1 | Negative stain. Representative micrographs and 2D classes for **a**, $MTHFR_{FL}$ incubated with 2.6 mM SAH and **b**, $MTHFR_{FL}$ incubated with 5 mM SAM. Both samples exhibit two conformations: one more extended conformation (upper rows) resembling the structure of $MTHFR_{trunc}^{SAH}$ (PDB:6fcx[16]) and one more compact conformation (lower rows) likely to represent inhibited MTHFR.

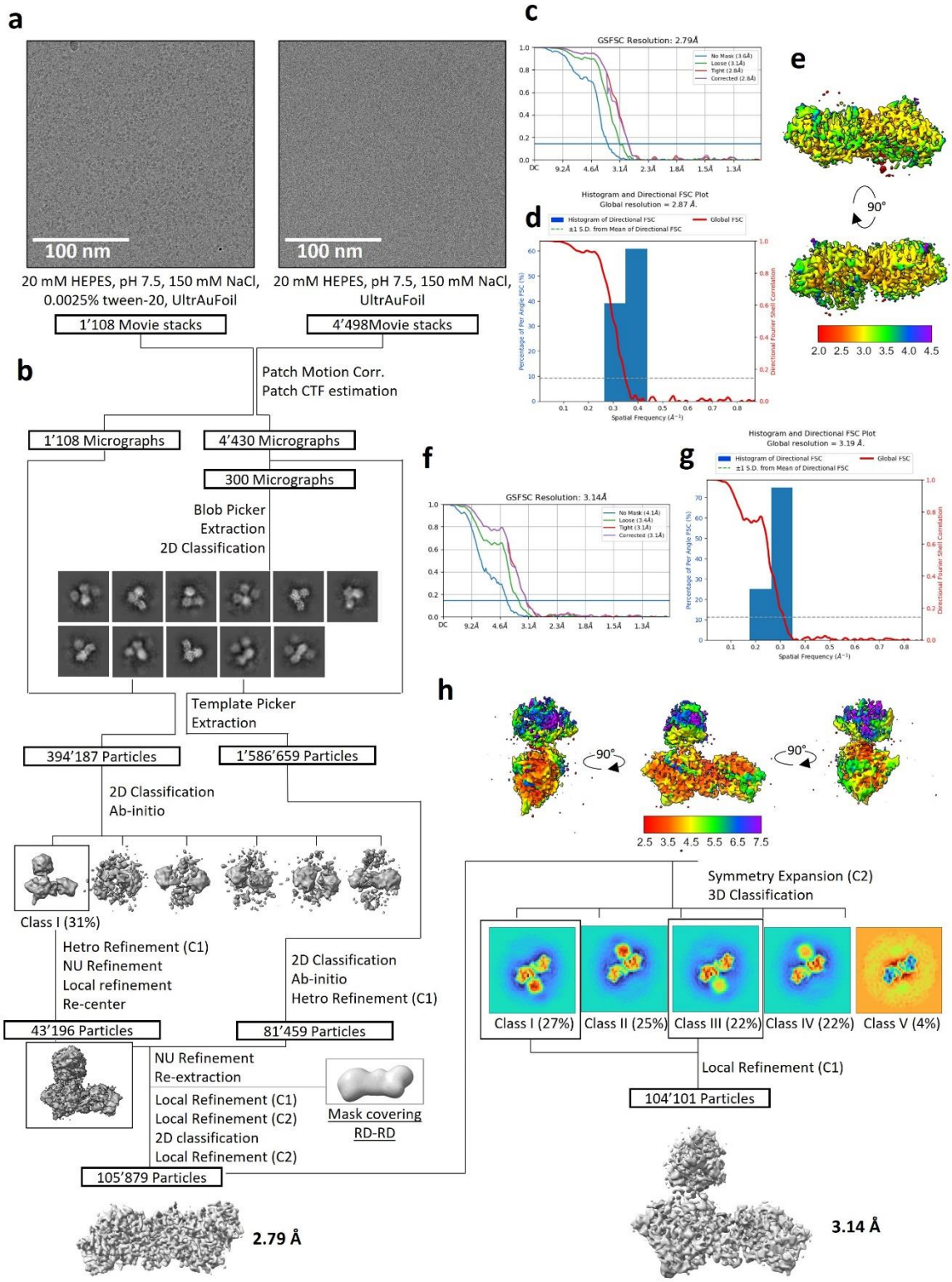

Extended Data Fig. 2 | Cryo-EM image processing workflow of $MTHFR_{FL}^{SAH}$. a, Representative micrographs from two movie stacks collected with different grid conditions. **b**, Process flow chart for pooled data sets from which two maps for $MTHFR_{FL}^{SAH}$ were reconstructed: One symmetric map $MTHFR_{FL}^{SAH\ (symm)}$ capturing the two regulatory domains at 2.79 Å with corresponding **c**, FSC curve **d**, 3D-FSC plot showing the angular distribution and **e**, local resolution distribution. One asymmetric map $MTHFR_{FL}^{SAH\ (asymm)}$ capturing the two regulatory domains and low-resolution volume, due to high flexibility, representing one

catalytic domain and linker region at average resolution of 3.14 Å, with corresponding **f**, FSC curve **g**, 3D-FSC plot showing the angular distribution and **h**, local resolution distribution.

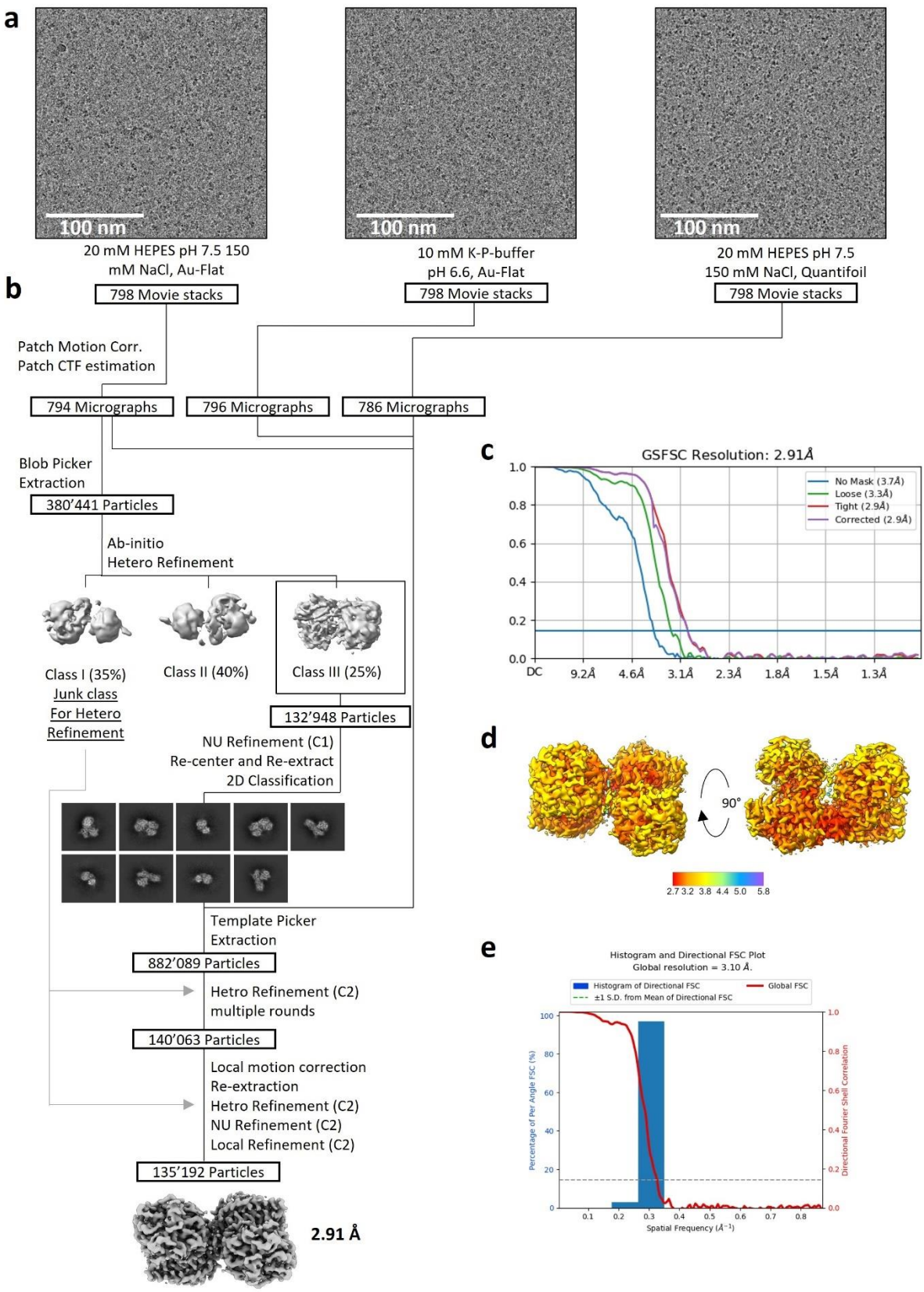

Extended Data Fig. 3 | Cryo-EM image processing workflow of $MTHFR_{FL}^{SAM}$. a, Representative micrographs from three movie stacks collected with different grid conditions. **b**, Process flow chart for pooled data sets from which one map for $MTHFR_{FL}^{SAM}$ at 2.91 Å

was reconstructed with corresponding **c**, FSC curve **d**, local resolution distribution. and **e**, 3D-FSC plot showing the angular distribution.

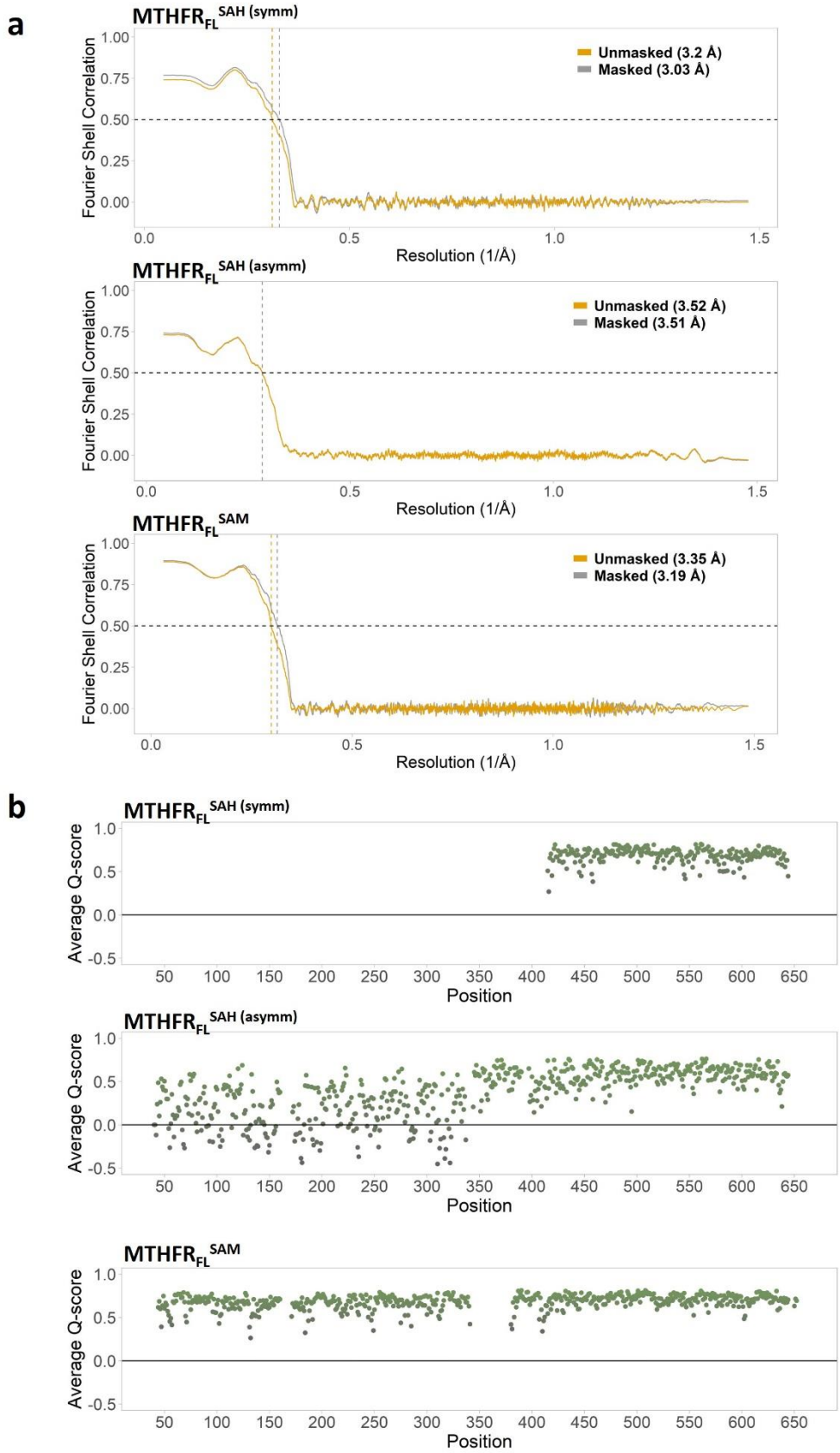

Extended Data Fig. 4 | Map and model quality of the MTHFR structures. a, Map to model FSC curves of the A-chains in $MTHFR_{FL}^{SAH\ (symm)}$, $MTHFR_{FL}^{SAH\ (asymm)}$, and $MTHFR_{FL}^{SAM}$ as determined by Phenix validation[50] with printed resolution at FSC=0.5. **b**, Average Q-score[52] for each amino acid position in the A-chains in $MTHFR_{FL}^{SAH\ (symm)}$, $MTHFR_{FL}^{SAH\ (asymm)}$, and $MTHFR_{FL}^{SAM}$. The low scores for residues 48 to 338 of $MTHFR_{FL}^{SAH\ (asymm)}$ are due to the low resolution of this region corresponding to the flexible CD.

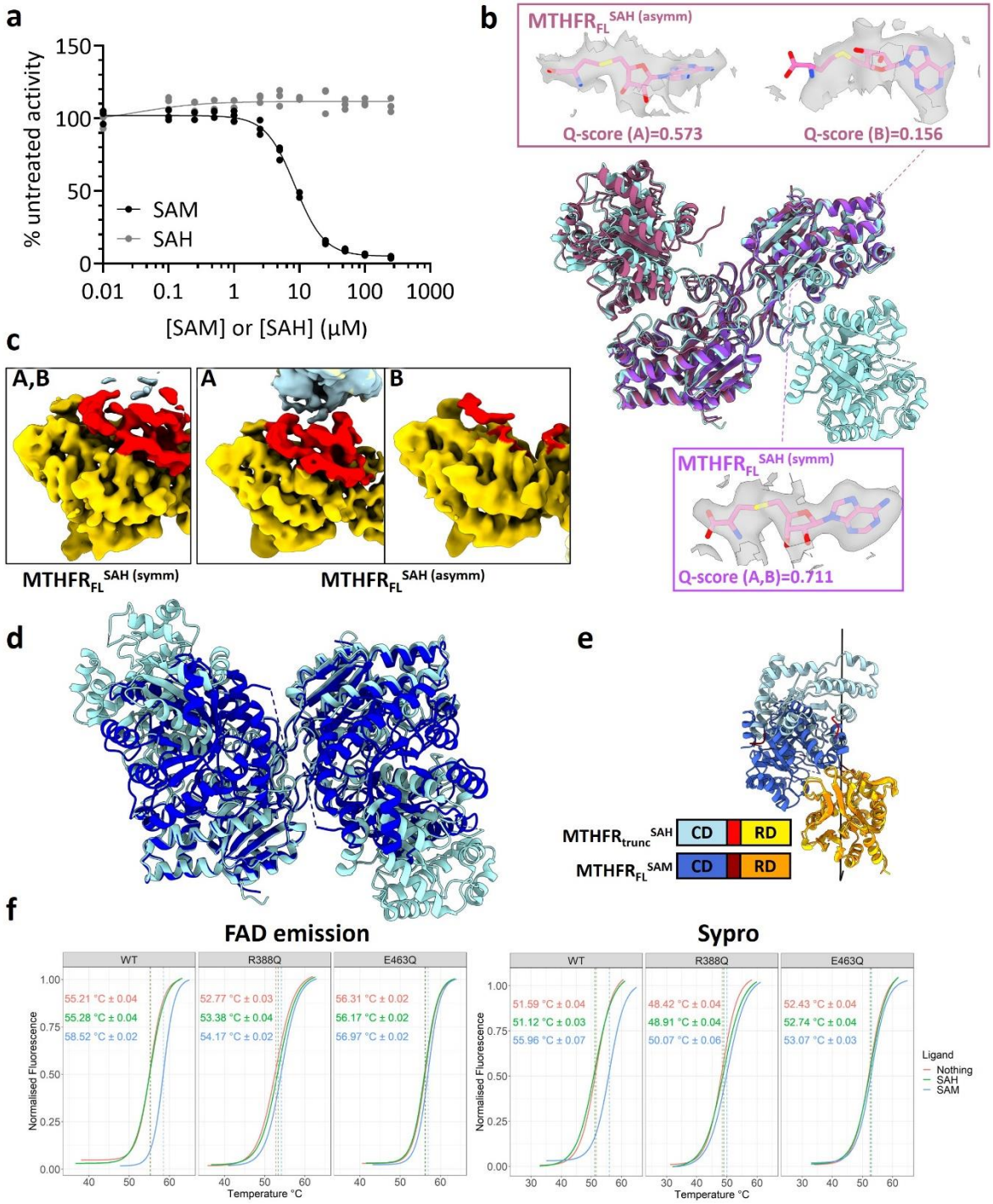

Extended Data Fig. 5 | Structural and biochemical response upon MTHFR$_{FL}$ binding SAM/SAH. a, Relative enzymatic activity of purified recombinant MTHFR$_{FL}$ following incubation with SAM or SAH. N=3 technical replicates. **b**, Cryo-EM models MTHFR$_{FL}$$^{SAH\ (asymm)}$ (dark pink) and MTHFR$_{FL}$$^{SAH\ (symm)}$ (purple) superimposed on MTHFR$_{trunc}$^{SAH} (light blue). Inset shows electron densities and Q-score for each SAH molecule in respective protomers (A, B). **c,** Zoomed view of the linker (red) with surrounding regulatory domain (yellow) and catalytic domain (blue) in respective protomer (A, B) of the cryo-EM maps MTHFR$_{FL}$$^{SAH\ (symm)}$ (left) and MTHFR$_{FL}$$^{SAH\ (asymm)}$ (middle and right) **d,** Cryo-EM model MTHFR$_{FL}$^{SAM} (dark blue) superimposed on MTHFR$_{trunc}$^{SAH} (light blue). **e**, Hinge axis generated with DynDom[54] comparing the relative position of the catalytic domain between MTHFR$_{FL}$^{SAM} (dark blue) and MTHFR$_{trunc}$^{SAH} (light blue). **f**, Differential fluorimetry of FAD

emission (left) or Sypro dye (right) of purified recombinant $MTHFR_{FL}$ or protein variants following incubation with 1 mM SAM, 1 mM SAH or no ligand. Tm calculated from inflation point was estimated using a Boltzmann curve fit function in R. N=6 technical replicates. Raw data found in Supplementary Data Fig. 1.

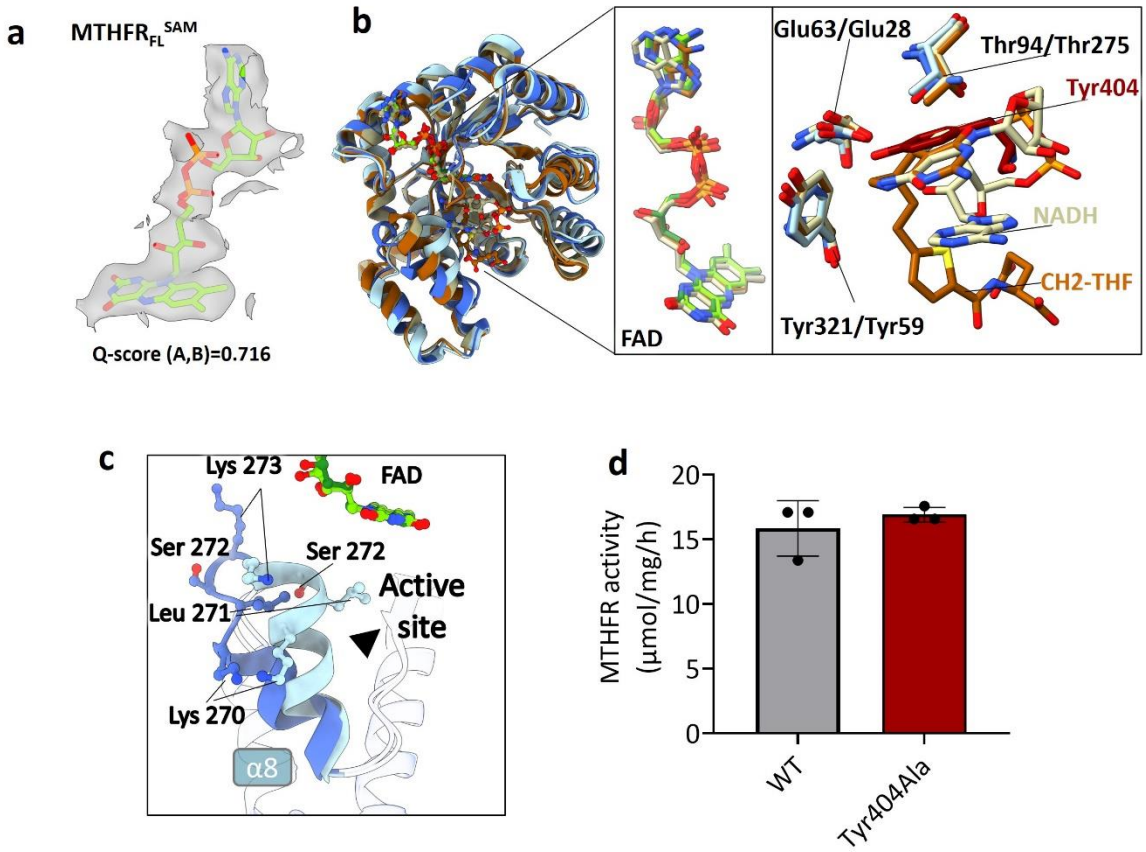

Extended Data Fig. 6 | The catalytic domain accommodates an auto-inhibitory element while maintaining a conserved structural integrity. a, Electron density and Q-score for FAD found in the respective protomer (A, B) of MTHFR$_{FL}^{SAM}$. **b**, Superimposition of human MTHFR$_{trunc}^{SAH}$ (light blue), human MTHFR$_{FL}^{SAM}$ (dark blue), *Escherichia coli* MTHFR co-crystallised with NADH (PDB:1zrq, beige), and *Escherichia coli* MTHFR co-crystalized with CH_2-THF (PDB:2fmn, brown). Inset showing a zoomed view of FAD (left) and residues interacting with Tyr404 (dark red) within the active site. **c**, [55,56]Zoomed view of superimposed MTHFR$_{trunc}^{SAH}$ (light blue) and MTHFR$_{FL}^{SAM}$ (dark blue) showing the movement of alpha helix 8 (α8) to accommodate hydrophobic linker insertion in the active site. **d**, Specific activity of overexpressed MTHFR$_{FL}$ (WT) and alanine substitution of Tyr404. N=3 technical replicates.

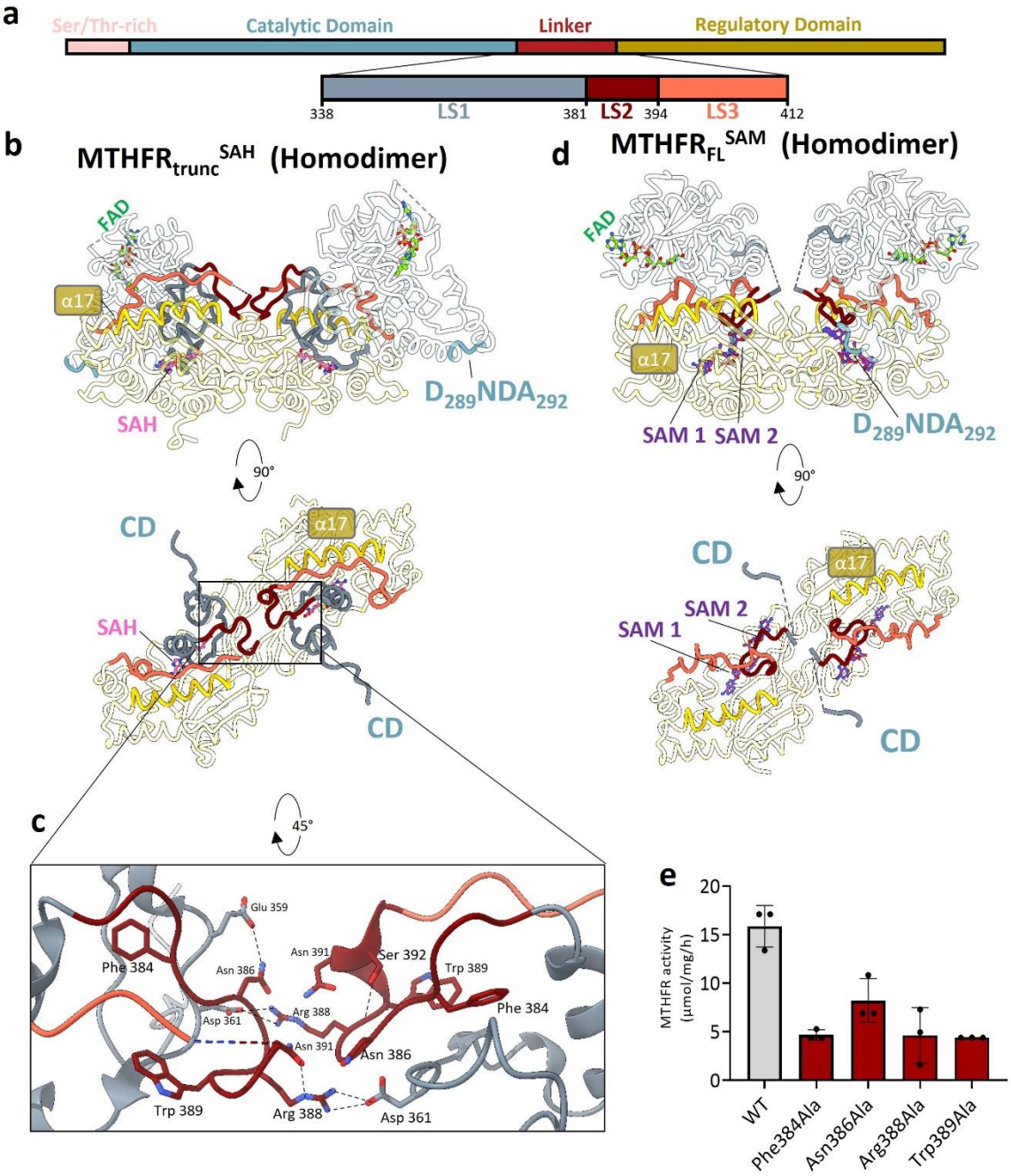

Extended Data Fig. 7 | Rearrangement of linker segments LS1, LS2 and LS3. a, Domain diagram of human MTHFR$_{FL}$, coloured according to MTHFR protein domains and with a zoom-in of linker segments LS1 (aa 338-380), LS2 (aa 381-393) and LS3 (aa 394-412). The same colour coding is maintained in subsequent structural representations **b, c, and d.** Transparent models of dis-inhibited MTHFR$_{trunc}^{SAH}$ (**b**) and inhibited MTHFR$_{FL}^{SAM}$ (**d**) with pronounced linker segments LS1, LS2 and LS3, showing their movement in relation to alpha-helix 17 (α17) and CD segment D$_{289}$NDA$_{292}$. **c**, Inset showing a zoom-in of the homodimeric interface in MTHFR$_{trunc}^{SAH}$, which is further stabilised by interactions between opposing LS2 in the two protomers. **e**, Specific activity data for overexpressed MTHFR$_{FL}$ and alanine substitutions within LS2. N=3 technical replicates.

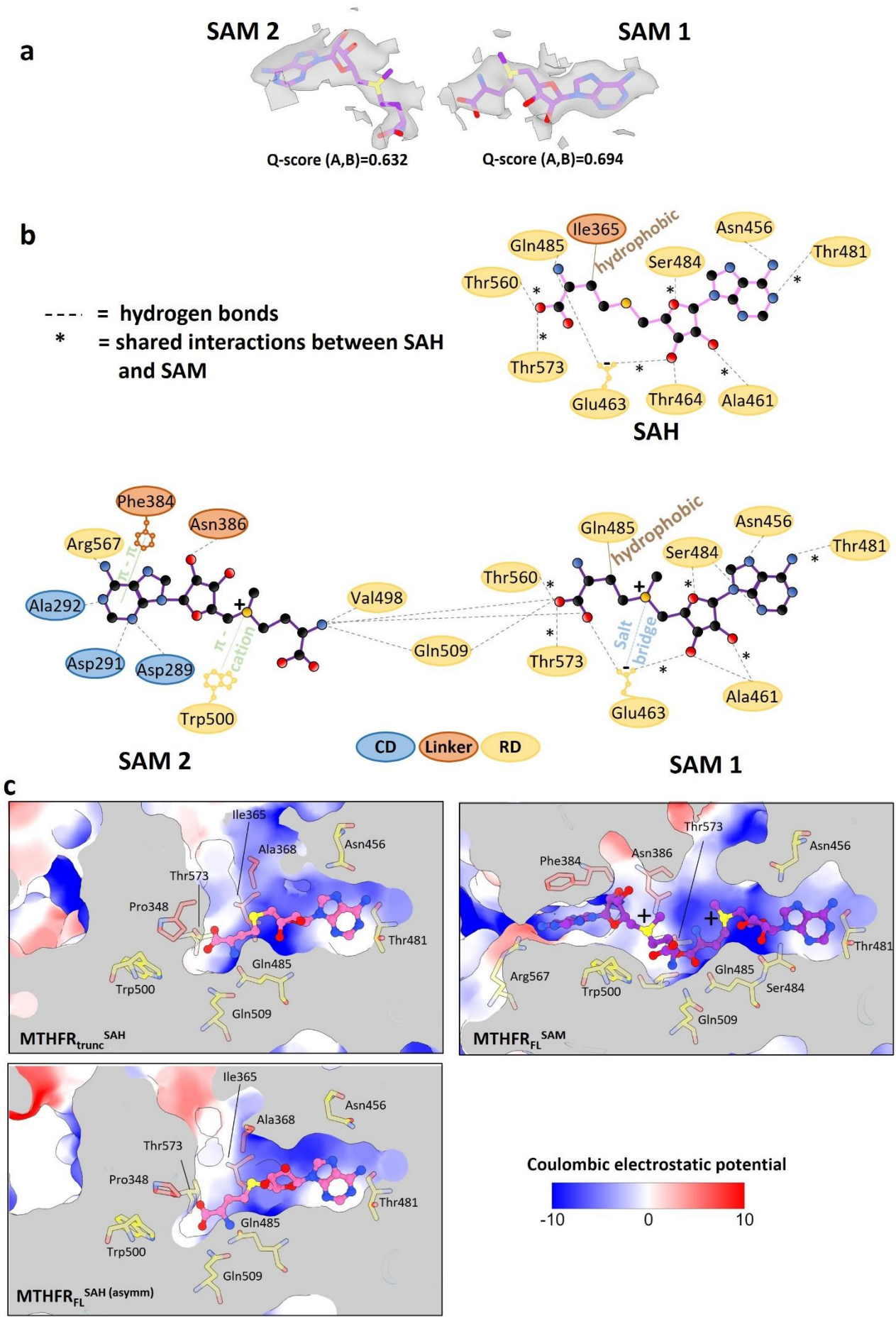
a
SAM 2
SAM 1
Q-score (A,B)=0.632
Q-score (A,B)=0.694
b
= hydrogen bonds
* = shared interactions between SAH and SAM
Ile365
hydrophobic
Gln485
Asn456
Thr481
Ser484
Thr560
Thr573
Glu463
Thr464
Ala461
SAH
Phe384
Asn386
Arg567
π - π
Ala292
Val498
π - cation
Gln509
Asp291
Asp289
Trp500
Salt bridge
CD
Linker
RD
SAM 2
SAM 1
c
Ile365
Ala368
Asn456
Thr573
Pro348
Thr481
Gln485
Trp500
Gln509
MTHFR trunc SAH
Phe384
Asn386
Arg567
Ser484
MTHFR FL SAM
MTHFR FL SAH (asymm)
Coulombic electrostatic potential
-10
0
10

983

Extended Data Fig. 8 | Structure and properties of the allosteric pocket. a, Electron density and Q-score for SAM1 and SAM2 in $MTHFR_{FL}^{SAM}$. **b**, Schematic depicting interactions within the allosteric pocket of $MTHFR_{trunc}^{SAH}$ for SAH, and within $MTHFR_{FL}^{SAM}$ for SAM1 and SAM2. Indicated interactions were predicted by PLIP[55], except for the hydrogen bond between SAM1 and SAM2, which were predicted by ChimeraX[44].**c**, Allosteric pocket for $MTHFR_{trunc}^{SAH}$, $MTHFR_{FL}^{SAH}$ and $MTHFR_{FL}^{SAM}$ with coulombic charge predicted with ChimeraX. Negative values in blue and positive in red, showing bound SAH (left) or SAM1 and SAM2 (right).

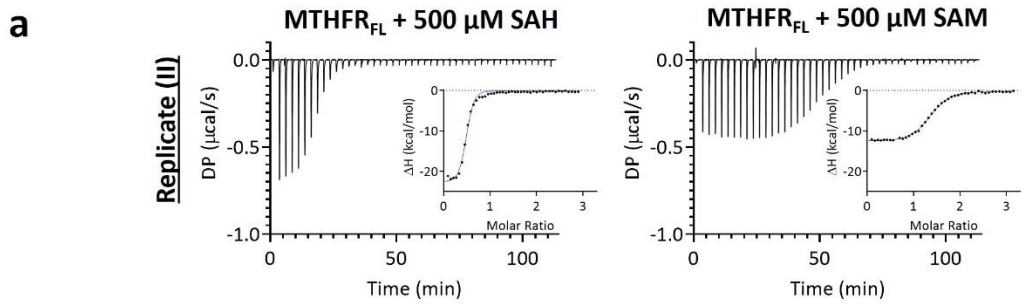

45 injections								
Sample	N ± error	Average ± S.D.	KD ± error (µM)	Average ± S.D.	ΔH ± error (kcal/mol)	Average ± S.D.	-TΔS (kcal/mol)	Average ± S.D.
MTHFR$_{FL}$ + SAM (I)	1.35 ± 0.00	1.33 ± 0.02	0.86 ± 0.04	0.93 ± 0.07	-12.80 ± 0.07	-12.95 ± 0.15	4.48	4.70 ± 0.22
MTHFR$_{FL}$ + SAM (II)	1.31 ± 0.01		0.99 ± 0.08		-13.10 ± 0.13		4.92	
MTHFR$_{FL}$ + SAH (I)	0.48 ± 0.00	0.47 ± 0.01	0.38 ± 0.03	0.38 ± 0.00	-23.70 ± 0.20	-23.40 ± 0.30	15.00	14.65 ± 0.35
MTHFR$_{FL}$ + SAH (II)	0.47 ± 0.00		0.39 ± 0.04		-23.10 ± 0.28		14.30	

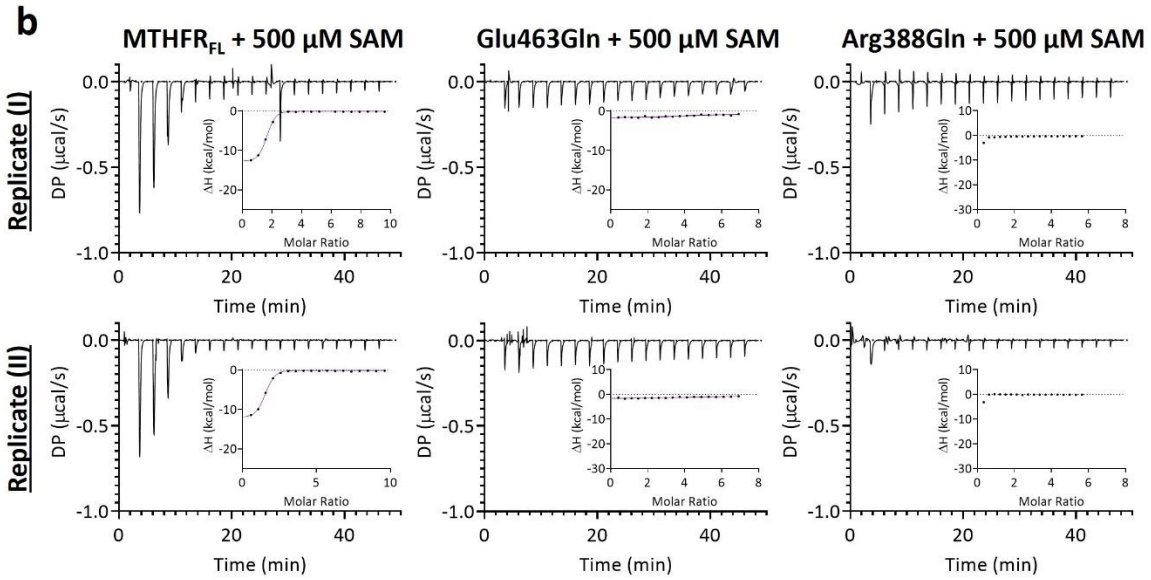

19 injections								
Sample	N ± error	Average ± S.D.	KD ± error (µM)	Average ± S.D.	ΔH ± error (kcal/mol)	Average ± S.D.	-TΔS (kcal/mol)	Average ± S.D.
MTHFR$_{FL}$ + SAM (I)	1.44 ± 0.02	1.40 ± 0.05	0.42 ± 0.07	0.51 ± 0.09	-13.00 ± 0.27	-12.65 ± 0.35	4.33	4.09 ± 0.24
MTHFR$_{FL}$ + SAM (II)	1.35 ± 0.02		0.59 ± 0.07		-12.30 ± 0.22		3.85	
E463Q + SAM (I)	7.67 ± 1.05	7.74 ± 0.07	27.60 ± 32.2	26.90 ± 0.70	-2.13 ± 0.58	-2.08 ± 0.05	-4.09	-4.16 ± 0.07
E463Q + SAM (II)	7.81 ± 0.97		26.20 ± 26.4		-2.02 ± 0.45		-4.23	
R388Q + SAM (I)	N/A	N/A	N/A	N/A	N/A	N/A	N/A	N/A
R388Q + SAM (II)	N/A		N/A		N/A		N/A	N/A

Extended Data Fig. 9 | Isothermal Titration Calorimetry. Isothermal titration calorimetry (ITC) experiments displaying the heat exchange over time. DP: power differential. The insets illustrate ΔH (change in enthalpy) plotted against the molar ratio. All curves have been normalized against buffer injected into respective MTHFR$_{FL}$ variants. **a,** Above: Shows 45 injections of 500 µM SAM or 500 µM SAH into 30 µM purified recombinant MTHFR$_{FL}$. N=2 technical replicates, where replicate I is shown in Fig. 4a. Below: Table of best-fit parameters (± corresponding fitting errors) for each replicate and the mean (± S.D.) for each sample condition. **b,** Above: Shows 19 injections of 500 µM SAM in 10 µM purified recombinant

$MTHFR_{FL}$ variants. N=2 technical replicates. Below: Table of best-fit parameters (± corresponding fitting errors) for each replicate and the mean (± S.D.) for each sample condition.

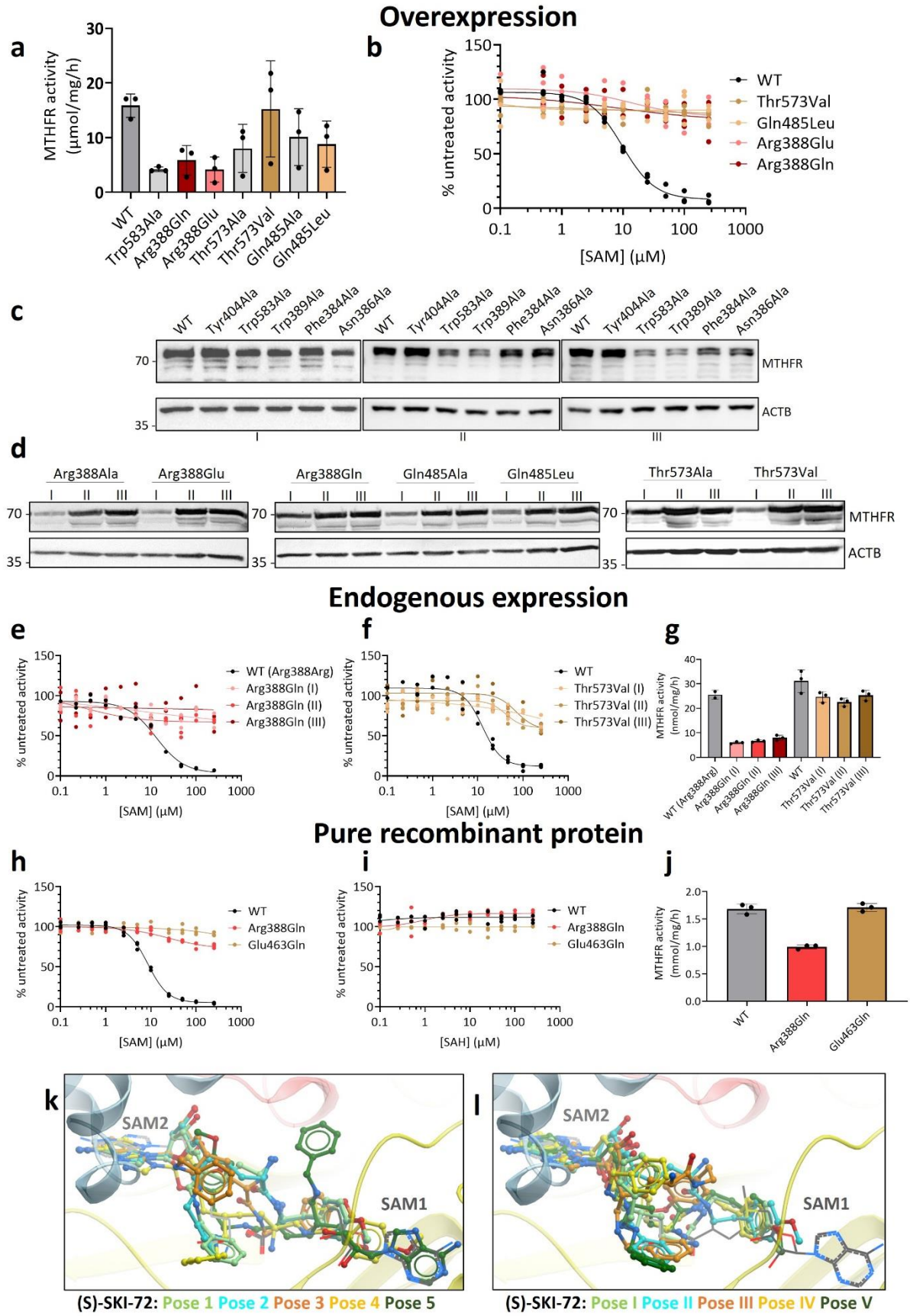

Extended Data Fig. 10 | Activity data for wild-type (WT) MTHFR and variants. Specific activity and inhibition curves (WT) MTHFR and protein variants overexpressed in MTHFR

knock-out 293T cells (**a-d**), genetically engineered for endogenous expression in 293T cells (**e-g**), or *as purified* recombinant **MTHFR$_{FL}$** protein following SF9 insect expression (**h-j**). **a**, Specific activity. **b**, Inhibition curves for variants Arg388Gln/Glu, Thr573Val and Gln485Leu with WT corresponding to WT seen in Fig. 2e and Fig. 4b,c. Western blotting analysis corresponding to all overexpressed proteins using **c,** 10% acrylamide gel and **d**, 12% acrylamide gel. N=3 biological replicates. **e-f**, Inhibition curves for endogenously expressed WT MTHFR and three clones each for **e**, Arg388Gln, and **f**, Thr573Val, generated with CRISPR/Cas9 gene editing. **g**, Specific activity for each. WT (Arg388Arg) represents a clone which had undergone CRISPR/Cas9 gene editing but showed no mutation within the MTHFR gene; WT represents the parental, unmodified 293T cells. N=3 technical replicates. **h-j**, Inhibition curves for purified recombinant MTHFR$_{FL}$ (WT) and variants Arg388Gln and Glu463Gln with **h,** SAM and **i**, SAH. **j**, Specific activity. N=3 technical replicates. **k-l**, Docking poses for (S)-SKI-72 docked into MTHFR structure solved in this work. Five poses were obtained each from docking performed after superimposing the adenine ring of (S)-SKI-72 with the equivalent substructure in either SAM1 (**k**) or SAM2 (**l**). Sticks are coloured according to ranking (1 – 5 for panel **k** and I – V for panel **l**) in light green, blue, orange, yellow and dark green respectively. Scores from different docking metrics are shown in Supplementary Table 1. Pose 5 from panel k and pose I from panel l are shown as representative poses in Figure 4d.